

Coupled motion of asymmetrical tilt grain boundaries: molecular dynamics and phase field crystal simulations

Z. T. Trautt,^a A. Adland,^b A. Karma^b and Y. Mishin^{a,*}

March 8, 2013

^a Department of Physics and Astronomy, MSN 3F3, George Mason University, Fairfax, VA 22030, USA

^b Department of Physics and Center for Interdisciplinary Research on Complex Systems, Northeastern University, Boston, MA 02115, USA

Abstract

Previous simulation and experimental studies have shown that some grain boundaries (GBs) can couple to applied shear stresses and be moved by them, producing shear deformation of the lattice traversed by their motion. While this coupling effect has been well confirmed for symmetrical tilt GBs, little is known about the coupling ability of asymmetrical boundaries. In this work we apply a combination of molecular dynamics and phase field crystal simulations to investigate stress-driven motion of asymmetrical GBs between cubic crystals over the entire range of inclination angles. Our main findings are that the coupling effect exists for most of the asymmetrical GBs and that the coupling factor exhibits a non-trivial dependence on both the misorientation and inclination angles. This dependence is characterized by a discontinuous change of sign of the coupling factor, which reflects a transition between two different coupling modes over a narrow range of angles. Importantly, the magnitude of the coupling factor becomes large or divergent within this transition region, thereby giving rise to a sliding-like behavior. Our results are interpreted in terms of a diagram presenting the domains of existence of the two coupling modes and the transition region between them in the plane of misorientation and inclination angles. The simulations reveal some of the dislocation mechanisms responsible for the motion of asymmetrical tilt GBs. The results of this study compare favorably with existing experimental measurements and provide a theoretical ground for the design of future experiments.

Keywords: Molecular dynamics, phase-field crystal, grain boundary, shear stress

*Corresponding author: ymishin@gmu.edu

1 Introduction

Recent research has led to the recognition that many grain boundaries (GBs) in crystalline materials can couple to applied shear stresses and are moved by them in a manner similar to dislocation glide [1–9]. During this “coupled” GB motion, the boundary produces shear deformation of the lattice and causes relative translation of the grains parallel to the GB plane. The coupling effect is characterized by a coupling factor β defined as the ratio of the tangential grain translation velocity $v_{||}$ to the normal GB velocity v_n : $\beta = v_{||}/v_n$. Coupling is considered perfect if β is a geometrically determined number depending only on crystallographic characteristics of the boundary and not on its velocity or the driving stress.

Initially observed experimentally for low-angle GBs in Zn [10, 11], the coupling effect has recently been demonstrated for many high-angle GBs in a number of metallic and non-metallic materials [6–9, 12–20]. The coupling can be responsible for the stress-induced grain growth in nano-crystalline materials [16, 21–24] and can influence the nucleation of new grains during recrystallization [25]. Molecular dynamics (MD) simulations have been effective in providing insights in the atomic mechanisms, geometric rules and dynamics of coupled GB motion [2–4, 21, 26–31]. It has also been found that the phase field crystal (PFC) methodology developed over the recent years [32–45] is well capable of reproducing equilibrium and non-equilibrium GB properties. In particular, it predicts reasonable values of GB energies [42] and has been able to reproduce the phenomenon of GB premelting [38, 39] as well as non-trivial structural transitions at GBs at high homologous temperatures [44]. In addition, it has been shown to reproduce the coupling effect for both two-dimensional (2D) [43] and 3D symmetric tilt boundaries [45].

Most of the experiments as well as simulations conducted so far have been focused on symmetrical tilt GBs. The less-studied case of asymmetrical tilt boundaries is more complex but poses new interesting questions. For example, low-angle symmetrical tilt GBs are known to move by collective dislocation glide in parallel slip planes [46]. By contrast, low-angle asymmetrical GBs are composed of at least two different types of dislocations. One would expect that the dislocations gliding in intersecting slip planes could block each other and prevent the coupled motion. In fact, the impossibility of coupled motion of asymmetrical boundaries was suggested in the classical paper by Read and Shockley [46]. Yet, recent MD simulations [31, 47, 48], bicrystal experiments [6, 9] and the observation of coupled GB motion in polycrystalline materials suggest that this may not be the case. Even less is known about geometric rules of coupling or migration mechanisms of large-angle asymmetrical GBs.

Based on purely geometric considerations, it was suggested that deviations of the GB plane from symmetric inclinations should preserve the coupled motion for both low and high-angle

GBs [4]. Furthermore, the coupling factor was predicted to be independent of the inclination angle as long as the coupling mode remains the same (see discussion of the multiplicity of coupling modes below) [4]. The MD simulations [47] of [001] tilt GBs in copper with the tilt angle $\theta = 18.92^\circ$ and several different inclinations showed that β did vary with the inclination angle within 10 to 20%. However, the boundary remained coupled over the entire angular range of inclinations as predicted. On the other hand, for large-angle boundaries with $\theta = 36.87^\circ$, two symmetrical and two asymmetrical boundaries were tested and the coupling factors were found to be different in both magnitude and sign (two β 's were positive and two negative) [47]. Zhang et al. [31] studied stress-driven motion of asymmetrical [001] tilt GBs in Ni with $\theta = 36.87^\circ$ and $\theta = 33.36^\circ$. They observed coupled motion (with varying sign of β) in some cases and sliding in other cases. The inconclusive and often conflicting results of the previous studies point to the need for a more detailed and systematic analysis of coupling of asymmetrical GBs.

In this paper we report on simulations of stress-driven motion of a large set of asymmetrical [001] tilt GBs by applying two complementary methodologies: MD and PFC. The MD simulations are conducted for specific materials (FCC copper and aluminum) and provide quantitative information about the mechanical stresses needed for driving the GB motion at different temperatures. The MD simulations are also well suited for studying atomic-level mechanisms of GB migration by examining atomic trajectories. A weakness of the MD approach is that the time scale is limited to tens of nanoseconds, preventing access to diffusion-controlled processes such as dislocation climb.

The PFC methodology overcomes, in principle, the latter limitation by permitting simulations on diffusive time scales, thereby describing both dislocation glide and climb [34]. This gives us the opportunity to get a glimpse into the possible GB behavior in the long-time regime which is currently inaccessible by MD simulations. However, one limitation of the PFC method is that the number of peaks of crystal density waves does not directly correspond to the number of atoms, which is not generally conserved. While this permits a description of dislocation climb phenomenologically, it remains unclear how to define and control the vacancy concentration in the PFC model. Theoretical attempts have been made to incorporate vacancies explicitly in the PFC model, but they do not fully resolve this issue since climb remains possible even for a vanishing vacancy concentration [49]. As a consequence, even though the geometrical aspects of the glide-mediated conservative GB motion are well modeled by PFC quantitatively, the description of non-conservative climb-mediated motion remains largely qualitative.

Despite this limitation, we find here that the MD and PFC approaches reveal remarkably similar coupling behaviors as a function of the misorientation and inclination angles, including the existence of a narrow transition region between two coupling modes and a sliding-like behavior

in this transition region. Hence, a comparison of the MD and PFC simulations helps us shed light on aspects of GB behavior that do not depend sensitively on detailed atomic mechanisms. Finally, in order to be able to explore efficiently the entire parameter space of the misorientation and inclination angles, we restrict our PFC simulations to 2D GBs between square lattices. We make use of the PFC model of Ref. [41], which energetically favors the square and FCC lattices in 2D and 3D, respectively. Even though the 2D square geometry is simpler than the 3D FCC structure studied in the MD simulations, we are able to quantitatively relate the Burgers vector character of the GBs in the PFC and MD simulations owing to the fact that the square lattice rotated by 45° is identical to one plane of the FCC lattice. Hence, the choice of the 2D geometry is not highly restrictive for the purposes of the present study.

2 Simulation geometry

The geometry of asymmetrical $[001]$ tilt GBs between FCC crystals is illustrated in Fig. 1. Because the orientations of the GB plane and the tilt axis are fixed, the system has two geometric degrees of freedom. These degrees of freedom can be associated with the tilt angle θ and the inclination angle ϕ . The tilt angle is defined as the misorientation angle between the $[001]$ directions in the grains, with $\theta = 0$ corresponding to a single crystal and $\theta \geq 0$ to the $[001]_1$ axis rotated in the counter-clockwise direction relative to $[001]_2$. The inclination angle ϕ is defined as the angle between the GB plane and the internal bisector between the $[001]$ directions in the grains. We take $\phi \geq 0$ if the bisector is rotated in the counter-clockwise direction relative to the GB plane. The case of $\phi = 0$ with $\theta \neq 0$ corresponds to a symmetrical tilt GB.

Due to the fourfold symmetry of the FCC lattice, all distinct GB structures can be found in the angular domain $\{0 \leq \theta < \pi/4, 0 \leq \phi < \pi/4\}$. However, we are interested in not only the GB structures but also their orientations relative to the laboratory coordinate system xyz (Fig. 1). In order to include all possible orientations of the GB structures, we consider an expanded domain $\{0 \leq \theta < \pi/2, -\pi/4 \leq \phi < \pi/4\}$.

Symmetry analysis gives the following orientation relationships between the GB structures:

$$(\theta, \phi) \xrightarrow{m_y} (\theta, -\phi), \quad (1)$$

$$(\theta, \phi) \xrightarrow{m_x} (90^\circ - \theta, 45^\circ - \phi), \quad \phi \geq 0, \quad (2)$$

$$(\theta, \phi) \xrightarrow{m_x} (90^\circ - \theta, -45^\circ - \phi), \quad \phi \leq 0. \quad (3)$$

Eq. (1) states that the GB structures with the same θ but opposite signs of ϕ are mirror reflections of each other across the GB plane (x, z) . Eqs. (2) and (3) state that replacement of the angles θ and ϕ by the complementary angles $(90^\circ - \theta)$ and $(\pm 45^\circ - \phi)$ reflects the GB structure across the mirror plane m_x normal to the x -axis. In particular, the inclination angles $\phi = \pm 45^\circ$ for a given θ produce identical symmetrical tilt boundaries which are m_x -reflections of the symmetrical boundary with $\phi = 0$ and the tilt angle $(90^\circ - \theta)$. As will be discussed later, these symmetry relations impose certain conditions on the response of the GBs to applied shear stresses. The symmetry relations (1)-(3) also apply to the 2D GBs modeled by the PFC method with an appropriate choice of the lattice unit cell.

3 Multiplicity of coupling modes

When a GB executes coupled motion, its dislocation content shears the lattice swept by its motion and simultaneously rotates the lattice to align it with the lattice of the growing grain. This combination of shear and rotation produces relative translation of the two grains parallel to the GB plane by the amount βL , where L is the normal GB displacement. As was discussed in previous work [2–4], the coupling factor β is a multi-valued function of the crystallographic angles of the boundary. There are two ways to understand the origin the multiplicity of coupling factor.

One way is to recognize that the shear deformation produced by the GB depends on its dislocation content, which, for a general GB, is defined by the Frank-Bilby equation [50]. The latter is known to have multiple solutions due to the crystal symmetry, leading to the multiplicity of dislocation content of the GB. Different dislocation contents produce different deformations of the lattice, which is manifested in different coupling factors observed during the boundary motion. This results in the existence of multiple coupling modes of the same GB, each corresponding to a different solution of the Frank-Bilby equation.

Another interpretation of the coupled motion focuses on the lattice rotation step. Consider a tilt GB as an example. To ensure continuity of the lattice of the growing grain, the receding lattice must be rotated around the tilt axis by the angle $\pm\theta$ (the sign depends on the direction of GB motion). However, if the lattice possesses n -fold rotation symmetry around the tilt axis, then rotations by the angles $\pm\theta + (2\pi/n)$, $\pm\theta + 2(2\pi/n)$, etc., also produce physically identical states of the growing grain. But these different rotation angles lead to different relative translations of the grains and thus different coupling factors.

For the [001] tilt axis in a cubic material, the fourfold symmetry generates four possible coupling modes, with the coupling factors $\beta = 2 \tan(\theta/2 + \pi k/4)$, $k = 0, 1, 2, 3$. In reality,

only two of them, corresponding to the smallest magnitude of β , have been observed in MD simulations [2–4] and experiments [6, 15, 18–20]. These two modes are referred to as $\langle 100 \rangle$ and $\langle 110 \rangle$ type and are characterized by the coupling factors

$$\beta_{\langle 100 \rangle} = 2 \tan \left(\frac{\theta}{2} \right) \quad (4)$$

and

$$\beta_{\langle 110 \rangle} = 2 \tan \left(\frac{\theta}{2} - \frac{\pi}{4} \right), \quad (5)$$

respectively. Note that these two coupling factors have different signs and describe GB motion in opposite directions in response to the same shear. For symmetrical tilt boundaries, the coupling factors obtained by simulations [2–4] and experiments [6, 15, 18–20] accurately follow the $\langle 100 \rangle$ mode for angles $\theta < 36^\circ$ and the $\langle 110 \rangle$ mode for angles $\theta > 36^\circ$. At the critical angle of approximately 36° , β abruptly changes from one mode to the other and can exhibit a “dual behavior” in which the boundary switches back and forth between the two modes [2–4]. It should be noted that this switching angle is not prescribed by any symmetry requirements and its exact value may depend on the material and/or the crystal structure. In particular, in a previous MD study of Cu [4], an examination of the gamma-surfaces for different coupling modes (Fig. 24 in [4]) revealed that the slip responsible for the $\langle 100 \rangle$ mode is more difficult than the slip corresponding to the $\langle 110 \rangle$ mode. The lower Peierls-Nabarro (PN) barrier for slip in the $\langle 110 \rangle$ mode is consistent with the fact that this mode spans a larger range of misorientation, and therefore that the switching angle is less than 45° .

We now discuss the coupling factors of asymmetrical tilt GBs. Suppose, as suggested in [2–4], the coupling factor for a given mode is independent of the inclination angle. Then one can hypothesize that the expected angle dependence of β would look as shown schematically in Fig. 2. Only the $\langle 100 \rangle$ and $\langle 110 \rangle$ modes are considered and their coupling factors are represented by two surfaces. The cut between the surfaces corresponds to the discontinuous transition between the modes accompanied by a reversal of sign. The exact shape of this cut is unknown and it is drawn in this figure with the only requirement that it respect the symmetry relations (1)-(3). When applying these relations, it was taken into account that the reflection of the GB structure across its plane (x, z) does not affect the coupling factor. By contrast, reflection of the GB structure across the mirror plane m_x normal to the x -axis reverses the sign of β . In particular, if for symmetrical boundaries with $\phi = 0$ the mode switching occurs at a tilt angle of $\theta = 36^\circ$, then for symmetrical boundaries with $\phi = \pm 45^\circ$ it occurs at $\theta = 90^\circ - 36^\circ = 54^\circ$. Accordingly, all boundaries with $\theta < 36^\circ$ are expected to have the same positive coupling factor, given by Eq. (4), regardless of ϕ . Likewise, all boundaries with $\theta > 54^\circ$ are expected to have the same

negative coupling factor given by Eq. (5) regardless of ϕ . For boundaries with $36^\circ < \theta < 54^\circ$, β is positive at and near $\phi = 0$ but is expected to switch to negative values when approaching $\phi = 45^\circ$ and $\phi = -45^\circ$. Although the exact switching angles may depend on the material, this analysis gives rather definitive qualitative predictions that can be tested by simulations.

It should be emphasized again that the shape of the cut between the surfaces in the putative diagram of Fig. 2, and even its existence, are at this point hypothetical. It is the goal of this paper to test this diagram by simulations. Our simulation results reported later in this paper will reveal that this diagram is qualitatively correct in identifying the overall shape of regions of opposite signs of β . However, we will see that it fails to capture the fact that the magnitude of β depends on the inclination angle and can become very large near the discontinuous boundary between the two coupling modes.

4 Methodology of atomistic simulations

Atomic interactions were modeled using embedded-atom method (EAM) potentials fit to experimental and first-principle data for Cu and Al [51, 52]. Both potentials accurately reproduce physical properties of these metals that are important in the context of this study. In particular, they predict accurate values of the elastic constants and stacking fault energies as well as dislocation core structures. The melting points predicted by these potentials are $T_m = 1327$ K for Cu and $T_m = 1040$ K for Al (the experimental values are 1357 K and 933 K, respectively). It should be noted that Al and Cu have significantly different stacking-fault energies and thus different dislocation core splittings and mobilities. The inclusion of both metals under the same methodology was intended to lend this work more generality and facilitate comparison with possible future experiments.

The GBs were created by constructing two separate crystals and joining them along a plane normal to the y -direction (Fig. 1). Periodic boundary conditions were imposed in the x - and z -directions parallel to the GB plane. To achieve commensurability of lattice plane periodicities in the grains in the x - and z -directions, the angles θ and ϕ were chosen so that to create a coincident site lattice (CSL) and align one of the CSL planes with the GB plane. The dimensions of the simulation block in the x - and z -directions comprised integral numbers of CSL periods, which completely eliminated coherency strains. In the y -direction, the grains were terminated at free surfaces. Several atomic layers near each surface were exempt from the MD process and were used only to control the boundary conditions. Namely, atoms in surface layer 2 were fixed in their perfect lattice positions during all simulations, whereas atoms in surface layer 1 were fixed only in the y - and z -directions and were displaced with the same constant velocity in the x -

direction. All other atoms were dynamic. Approximate dimensions of the simulation block were $L_X \approx 100\text{-}200\text{\AA}$, $L_Y \approx 370\text{\AA}$ and $L_Z \approx 37\text{\AA}$ and the total number of atoms was 1×10^5 to 2×10^5 .

The equilibrium GB structure was obtained by the energy minimization procedure described in [53]. Prior to the MD simulation, the block was uniformly expanded by the thermal expansion factor at the chosen simulation temperature. This expansion was intended to eliminate thermal stresses inside the grains. The thermal expansion factors for EAM Cu and Al were known from separate calculations [27, 51]. The MD simulations were performed in the canonical (NVT) ensemble with temperature controlled by a Nose-Hoover thermostat. A 2 femtosecond time integration step was used throughout this study. After temperature reached the target value, the GB was equilibrated by an isothermal anneal for a few hundred picoseconds. The equilibration was followed by a production run in which the surface layer 1 was moved parallel to the x -direction with the speed of $v = 0.5$ m/s, imposing a shear strain rate of about 10^7 s $^{-1}$. Shears in both positive and negative x -directions were implemented for each boundary. The production runs took up to 50 nanoseconds but were often terminated earlier when the GB reached one of the surface layers (Fig. 1). Multiple snapshots of the simulation block containing the coordinates of all atoms, their energies and other relevant information were saved during the simulations.

The following technique was applied for tracking the GB motion. First, an orientation parameter, λ , was assigned to each individual atom in a given snapshot. To this end, vector positions \mathbf{r}_{ij} of $n \approx 50$ nearest neighbors of a chosen atom i were compared with positions $\hat{\mathbf{r}}_m(\alpha)$ of 12 first-nearest neighbors of an atom in the perfect FCC lattice rotated by an angle α around [001]:

$$\psi_i(\alpha) = \sum_{j=1}^n \sum_{m=1}^{12} \sum_{k=1}^3 \exp \left[-\frac{(r_{ijk} - \hat{r}_{mk}(\alpha))^2}{a^2} \right]. \quad (6)$$

Here a is the equilibrium lattice constant and index k runs over three Cartesian components of a vector. The quantity $\psi_i(\alpha)$ was calculated for two angles α corresponding to the chosen rotations of the grains relative to the coordinate system. The angle with the larger $\psi_i(\alpha)$ provided a better match between the actual and ideal lattice orientations and was assigned to atom i as its orientation parameter λ . Fig. 3 illustrates this procedure by showing the atoms assigned to the grains by the bright and dark colors.

After partitioning the atoms between the grains, the mean GB position h was calculated as $h = L_Y N / N_0$, where N is the number of atoms in grain 1 and N_0 is the total number of atoms in the simulation block. The plots of h versus time were used for calculation of the coupling factor β . The first and last 15 \AA of the plot were disregarded to eliminate the effects of the elastic strain and interaction with the surface layers. The remaining part of the plot was linearized by a

least-mean-square fit and the slope S of the regression line was used to compute $\beta = v/S$.

Various visualization methods were applied for examining the structures of moving GBs. In particular, for GBs composed of discrete dislocations their slip traces contained information about the dislocation movements and reactions. The deformation fields method proposed in [54] was implemented and applied for visualization of dislocations and their slip traces during the GB motion.

5 Methodology of PFC simulations

The PFC model is generally formulated as an evolution equation for the dimensionless crystal density field $\psi(\vec{r}, t)$ defined as the departure of the atomic number density $n(\vec{r}, t)$ from some reference value n_0 normalized by that value, $\psi(\vec{r}, t) = (n(\vec{r}, t) - n_0)/n_0$. Here PFC simulations are carried out in the grand canonical ensemble with a constant chemical potential μ , so that ψ is a non-conserved field. We use the dynamical formulation [40]

$$\frac{\partial^2 \psi}{\partial t^2} + \alpha \frac{\partial \psi}{\partial t} = -\frac{\delta F}{\delta \psi} + \mu, \quad (7)$$

where the second order partial derivative with respect to time, $\partial^2 \psi / \partial t^2$, has the advantage of rapidly relaxing the elastic field via propagation of wave-like modes that mimic phonons in a real solid. The first order partial derivative with respect to time damps those modes and also models diffusive processes. The total free-energy of the system is expressed in terms of the functional

$$F = \int d\vec{r} f + F_{ext}, \quad (8)$$

where f is the free-energy density of the bulk crystal chosen to have the form [41]

$$f = \frac{\psi}{2} (-\epsilon + (\nabla^2 + 1)^2 [(\nabla^2 + Q_1^2)^2]) \psi + \frac{\psi^4}{4}, \quad (9)$$

and F_{ext} specified below models an “external” potential used to shear the system. The form of f couples two sets of crystal density waves with different reciprocal lattice vectors, where Q_1 is the ratio of the magnitudes of those vectors. This form models FCC lattices in 3D by coupling $[111]$ and $[200]$ reciprocal lattice vectors with $Q_1 = \sqrt{4/3}$, and square lattices in 2D by coupling $[10]$ and $[11]$ reciprocal lattice vectors for the choice $Q_1 = \sqrt{2}$, which is adopted here.

As in the MD simulations, the GBs were created by constructing two separate crystals and joining them along a plane normal to the y -direction (Fig. 1). We use identical definitions and sign conventions for the tilt and inclination angles as in the MD simulations. Periodic boundary

conditions were applied in the x -direction, with the angles θ and ϕ and the dimension L_X chosen to be equal to an integral number of CSL periods in order to eliminate coherency strains in the crystals. The dimension L_Y was chosen to be large enough to obtain GB behaviors that are independent of L_Y , with typical values in the range of 100 lattice spacings.

To enable comparison between the PFC and MD results, we replaced the primitive square unit cell of the 2D PFC lattice with edge a by an expanded unit cell rotated by 45° with edge $\sqrt{2}a$, which contains 2 atoms (Fig. 4). As a result, the PFC structure becomes identical up to a scaling factor to one of the (002) crystal planes of the 3D FCC structure. With this choice of the unit cell, the Burgers vectors of the two types of dislocations present in the MD and PFC lattices have the same Miller indices: $\langle 100 \rangle$ and $1/2\langle 110 \rangle$ in MD and $\langle 10 \rangle$ and $1/2\langle 11 \rangle$ in the PFC simulations, respectively. Henceforth, all crystallographic indices related to the PFC structures will be given with respect to the expanded unit cell. Fig. 4 illustrates $1/2\langle 11 \rangle$ dislocations forming a low-angle symmetrical tilt GB. The Burgers vector is given by the closure failure of the Burgers circuit drawn around one of the dislocations.

Since the PFC method does not model a solid-vacuum interface, we cannot use free surfaces as in the MD simulations to shear the bicrystal. However, we can mimic free surfaces by choosing the chemical potential to vary spatially over narrow strips near the top and bottom surfaces of the crystal for the geometry depicted in Fig. 1. This is accomplished by choosing the chemical potential μ to vary spatially along the direction y normal to the GB from a value μ_s which favors the solid phase in most of the bulk of the sample to a value μ_l which favors the liquid phase near the top and bottom surfaces. With y varying from 0 to L_Y , where 0 corresponds to the bottom surface, the choice

$$\mu = \mu_l + \frac{(\mu_l - \mu_s)}{2} (\tanh [(y - L_Y + b)/\xi] - \tanh [(y - b)/\xi]) \quad (10)$$

melts the top and bottom surfaces a distance b into the sample if the parameter ξ is chosen much smaller than b . To determine the values of μ_l and μ_s , we first compute the solid-liquid phase diagram by a standard common tangent construction where the free-energy of the solid phase is computed by expanding the crystal density field in terms of the two sets of $[10]$ and $[11]$ density waves as described in [41]. This construction yields the value of the equilibrium chemical potential, μ_E , for solid-liquid coexistence. The solid (liquid) phase is favored for $\mu > \mu_E$ ($\mu < \mu_E$) on the side of the phase diagram where μ_E is negative and the average solid density is larger than the liquid density. We choose $\mu_s = 0.9\mu_E$ and $\mu_l = 1.1\mu_E$ for all simulations reported here.

A shear is imposed by choosing

$$F_{ext} = \int dx dy \left[G(y-d) (\psi(x,y,t) - \psi_0(x-vt,y))^2 + G(y-L_y+d) (\psi(x,y,t) - \psi_0(x+vt,y))^2 \right], \quad (11)$$

where $G(y) = \exp(-y^2/2\sigma^2)/\sqrt{2\pi\sigma^2}$ is a normalized Gaussian of width σ and $\psi_0(x,y)$ corresponds to the analytical expression for the equilibrium ψ field for a perfect single crystal approximated as a superposition of the $[10]$ and $[11]$ sets of crystal density waves (Eq. (87) in [41]). Since the dynamics tends to drive the system towards a minimum of the grand potential $F - \mu \int d\vec{r} \psi$, the terms proportional to $(\psi(x,y,t) - \psi_0(x \pm vt, y))^2$ in the integrand of F_{ext} tend to entrain ψ in a way that is equivalent to pulling the crystal in opposite directions along x at velocity $\pm v$. The Gaussian kernels enforce that this pulling only takes place in narrow strips of width σ centered at a distance d into the sample from its bottom and top surfaces. In general, d needs to be chosen much smaller than L_y and slightly larger than the width b of the surface melted layers so that the pulling is applied to solid strips near the bottom and top surfaces that are not melted.

All the simulations were carried out with $\alpha = 0.1$ and $v = 1.25 \times 10^{-4}$, where $2v$ is the relative velocity of the two crystals (cf. Eq. (11)). A series of simulations of symmetrical tilt boundaries and all the simulations of asymmetrical tilt boundaries were carried out with $\epsilon = 0.25$ for which $\mu_E = -1.33215$ (recall that $\mu_s = 0.9\mu_E$ and $\mu_l = 1.1\mu_E$ in Eq. (10)). We also repeated the series of simulations for symmetrical tilt boundaries with $\epsilon = 0.05$ and thus $\mu_E = -0.593103$. This choice was motivated by the fact that the discontinuous transition between the two different coupling modes is expected from the previous MD work [4] reviewed above to occur at a critical misorientation that is controlled by the relative magnitudes of the PN barriers to dislocation motion in different coupling modes. For the higher ϵ value ($\epsilon = 0.25$), the PN barrier turns out to be substantially larger for the $\langle 10 \rangle$ than $1/2\langle 11 \rangle$ dislocations [55]. Since low-angle symmetrical tilt boundaries with small θ are composed of $\langle 10 \rangle$ dislocations, the coupled motion is expected to switch from the $\langle 10 \rangle$ to the $\langle 11 \rangle$ coupling mode at a relatively low misorientation, i.e., at a misorientation that is large enough for $\langle 10 \rangle$ dislocation cores to overlap but smaller than 45° . By contrast, for the lower ϵ value, the PN barriers are much smaller and of comparable magnitude for the $\langle 10 \rangle$ and $1/2\langle 11 \rangle$ dislocations. In this case, one would expect the transition between the two coupling modes to occur at a misorientation angle close to 45° . Our PFC simulation results reported below will confirm these expectations by showing that the switching angle between the coupling modes is close to 20° when the PN barrier is much larger for $\langle 10 \rangle$ than for $1/2\langle 11 \rangle$ dislocations ($\epsilon = 0.25$) and comes close to 45° when both barriers are negligibly small ($\epsilon = 0.05$).

We note that the calculation of the PN barriers in PFC simulations requires choosing the shearing velocity v sufficiently small for the viscous-like stress associated with grain translation

(absent in the MD simulations and real solids) to be much smaller than the Peierls stress. Computation of this stress and reformulation of the PFC model to eliminate this spurious viscous stress will be discussed elsewhere [55]. What is important for the present study is that v was chosen small enough for the results not to depend on this PFC artifact.

The dynamical equations were solved using a pseudo-spectral scheme with a mesh spacing $\Delta x = \Delta y = 2\pi/8$ and a time step $\Delta t = 0.1$. This scheme extends the one described in [39] to treat the second order partial derivative in time in Eq. (7). Details of this scheme will be described elsewhere [45]. Since the edge of the square unit cell with one atom per cell is $a = 2\pi$ in dimensionless PFC units (and $\sqrt{2}a$ for the expanded unit cell with 2 atoms used for comparisons with MD), this choice of mesh spacing corresponds to having $8 \times 8 = 64$ mesh points per unit cell of the square lattice. For the parameters used to melt and pull the top and bottom surfaces of the crystal, we chose $b = 5a = 10\pi$, $\xi = 2a$, $\sigma = a = 2\pi$, and $d = 12a$.

6 Equilibrium grain boundary structures

Examples of equilibrium GB structures studied in this work are given in Figures 5 and 6. Fig. 5(a) shows an asymmetrical boundary with relatively small angles of $\theta = 16.26^\circ$ and $\phi = 14.04^\circ$. In the structure obtained by the MD simulations, individual GB dislocations can be easily distinguished and their Burgers vectors can be readily determined by the standard Burgers circuit construction. This boundary has a periodic structure comprising six $\langle 100 \rangle$ dislocations and four $1/2\langle 110 \rangle$ dislocations in each period. The core of each dislocation can be considered as a stack of identical structural units representing capped trigonal prisms in three dimensions. Their 2D projections appear as kites and are outlined in the figure in green color. The PFC simulations give a similar structure of this boundary, with the same number of dislocations of each type (Fig. 5(b)). The exact positions of the dislocations are different and vary with temperature and time. However, the dislocation content predicted by both methods is identical. In fact, all GBs with $\theta = 16.26^\circ$ studied in this work were found to be mixtures of these two types of dislocations in proportions dictated by the inclination angle. These proportions were found to be precisely the same in both MD and PFC simulations. In the particular case of $\phi = 0$, the boundary becomes symmetrical and its structure represents an array of $\langle 100 \rangle$ dislocations. Likewise, both methods confirm that the symmetrical boundaries with $\phi = \pm 45^\circ$ are composed of $1/2\langle 110 \rangle$ dislocations.

As examples of high-angle GBs, Figs. 6(a,b) show the structures of symmetrical boundaries with $\theta = 36.87^\circ$. This lattice misorientation produces a CSL known as $\Sigma 5$, Σ being the reciprocal density of coincident sites [50]. The structures shown in this figure are for the inclination angles $\phi = 0$ and $\phi = 45^\circ$, corresponding to the GB planes (310) and (210) , respectively. Both

structures are formed by topologically identical kite-shape structural units similar to those in Fig. 5(a). Such units are separated by one atomic bond when $\phi = 0$ and are connected head-to-tail when $\phi = 45^\circ$. The rows of such structural units running parallel to the tilt axis are similar to dislocation cores in low-angle boundaries and can be also considered as GB dislocations in high-angle boundaries.

Figure 6(c) illustrates a typical structure of an asymmetrical $\Sigma 5$ GB, with the inclination angle of $\phi = 14.04^\circ$. The kite-shape structural units “clustered” together or separated by a bond can be considered as patches (facets) of the symmetrical $\Sigma 5$ (210) ($\phi = 45^\circ$) and $\Sigma 5$ (310) ($\phi = 0$) boundaries, respectively.

The PFC simulations show similar structural trends of high-angle GBs. However, a detailed one-to-one comparison between the PFC and MD structures is limited because of their different dimensionality. In particular, the characteristic kite-shape structural units forming the 3D GBs include sites located in adjacent (002) planes. Such structural units have no analog in the 2D PFC structures containing only one layer.

7 Mechanisms of grain boundary motion

7.1 MD results

The mechanisms of GB motion will be discussed for relatively low-angle boundaries in which the evolution of individual dislocations could be reliably traced. Examination of MD snapshots revealed that the GB motion at low temperatures ($0.3T_m$ to $0.5T_m$) was accomplished by dislocation glide assisted by dislocation rearrangements and reactions. As mentioned in Section 1, stress-driven motion of symmetrical tilt GBs occurs by collective glide of identical dislocations along parallel slip planes [3, 4]. This motion does not require dislocation rearrangements or reactions. This mechanism was indeed observed in our simulations as illustrated in Fig. 7(a) for the boundary with $\theta = 16.26^\circ$ and $\phi = 0$.

In the case of asymmetrical GBs, the two types of dislocations forming the GB structure belong to different slip systems. After a period of time, the dislocations gliding in intersecting slip planes can create locked configurations preventing further GB motion. Nevertheless, our MD simulations have shown that the dislocations usually find a way to glide past each other without completely locking themselves. Fig. 7(b) illustrates the simultaneous glide of $\langle 100 \rangle$ and $1/2\langle 110 \rangle$ dislocation arrays during the motion of an asymmetrical boundary with $\theta = 16.26^\circ$ and $\phi = 38.66^\circ$. Note how the dislocation slip traces cross each other multiple times without locking.

Two mechanisms were identified by which the dislocations could avoid blocking each other while preserving the total Burgers vector. These mechanisms involve dislocation reactions and dislocation avoidance, respectively.

The dislocation reaction mechanism is similar to the one observed in the recent MD study of shrinkage and rotation of isolated cylindrical grains [28]. Fig. 8 schematically illustrates a typical dislocation reaction process in which a single $1/2 \langle 110 \rangle$ dislocation propagates through an array of $\langle 100 \rangle$ dislocations. The structure shown in this figure represents a typical asymmetrical GB with relatively small angles θ and $\phi < \theta$. At each step of this process, the $\langle 100 \rangle$ dislocation on the immediate right of the $1/2 \langle 110 \rangle$ dislocation dissociates in two $1/2 \langle 110 \rangle$'s. One of the product dislocations glides over a short distance (comparable to the dislocation spacing) and recombines with the initial $1/2 \langle 110 \rangle$ dislocation to form a new $\langle 100 \rangle$. The remaining product dislocation is similar to the initial $1/2 \langle 110 \rangle$ but is located a short distance to its right (compare configurations (a) and (g) in Fig. 8). This new configuration continues to propagate to the right by repeating the same steps: reaction of the $1/2 \langle 110 \rangle$ dislocation with a neighboring $\langle 100 \rangle$ and recombination with one of its products. This process looks as if the $1/2 \langle 110 \rangle$ dislocation migrated along the boundary to the right (compare the initial (a) and final (h) configurations in Fig. 8). However, it is only the $1/2 \langle 110 \rangle$ Burgers vector that propagates over many steps, whereas each individual dislocation glides only over a short distance. Note that this dislocation propagation process produces a slight displacement of the dislocation array down. Multiple dislocation passes can produce significant GB displacements. The remarkable feature of this mechanism is that it does not require dislocation climb, despite the fact that the propagating dislocation has a Burgers vector component normal to the GB plane.

A similar chain of reactions can propagate a $\langle 100 \rangle$ dislocation through an array of $1/2 \langle 110 \rangle$'s or $\langle 100 \rangle$'s, or a $1/2 \langle 110 \rangle$ dislocation through an array of $1/2 \langle 110 \rangle$'s. Such dislocation reactions provide a mechanism for rapid redistribution of dislocation content over the GB without altering the total dislocation content or relying on diffusion-controlled mechanisms such as climb. These dislocation reactions prevent the formation of locks and simultaneously provide a mechanism for GB motion.

The second mechanism was the dislocation avoidance. When the ratio of the numbers of the two type of dislocations was large, we observed that the minority dislocations tended to lag behind the majority dislocations and then return to the boundary when a suitable gap was available. This process is illustrated schematically in Fig. 9 for the dislocation ratio 2:1. First, the majority dislocations move forward while the minority dislocations are left behind. This separation of dislocations creates gaps in the array of majority dislocations. (Such gaps represent elastically distorted perfect lattice regions between terminations of dislocation arrays and can be

considered as disclination dipoles [56]). Then, when the slip planes of the minority dislocations come to alignment with the gaps, they quickly glide forward and fill the gaps, recreating the initial GB structure. As evident from the geometry of this process (Fig. 9), each minority dislocation fills a gap left by a neighboring minority dislocation. Thus, the net result of this process is similar to the dislocation reaction mechanism: both processes lead to relative translations of two dislocation arrays parallel to the GB plane without interfering with each other. Fig. 10 illustrates the dislocation avoidance mechanism for a particular GB with $\theta = 16.26^\circ$ and $\phi = 2.73^\circ$. This Figure shows that the minority dislocations do not necessarily fill all gaps simultaneously but can fill them one or several at a time.

The chains of dislocation reactions represent the dominant mechanism responsible for the motion of asymmetrical GBs. The dislocation avoidance mechanism was observed only for GBs with small inclinations and inclinations close to $\pm 45^\circ$, which contained large ratios of the different dislocation types (e.g., 10:1). In a small number of simulations at temperatures below $0.3T_m$, the dislocations formed strongly locked configurations. Such locks eventually triggered generation of new dislocations which initiated plastic deformation of the grains.

Similar mechanisms were found to operate in high-angle GBs, with rows of kite-shape structural units playing the role of dislocation cores.

7.2 PFC results

In the PFC simulations, the dislocations forming the GBs with relatively low angles could be readily identified and followed during the GB motion. As expected, symmetrical boundaries with $\phi = 0$ and $\phi = \pm 45^\circ$ migrated by glide of identical dislocations in their respective slip planes. Fig. 11 shows a typical dislocation trace during the motion of a GB with $\theta = 16.26^\circ$ and $\phi = 45^\circ$. This boundary is composed of $1/2 \langle 11 \rangle$ dislocations which glide in (11) planes. A more detailed picture of this process is illustrated in Fig. 12. The dislocation moves by a conservative process in which the structural units forming its core are continually distorted and converted to perfect-lattice units left behind the dislocation.

For asymmetrical GBs, however, the migration mechanisms are more complex. Typically, the majority dislocations glide in their respective slip planes as before, whereas the minority dislocations progress parallel to the *same* slip planes as the majority. This process is illustrated in Fig. 13 by dislocation traces in the asymmetrical GB with $\theta = 16.26^\circ$ and $\phi = 30.2^\circ$. This particular boundary contains one $\langle 10 \rangle$ dislocation per every three $1/2 \langle 11 \rangle$ dislocations. The majority dislocations move by perfect glide along (11) planes containing their Burgers vector. The minority $\langle 10 \rangle$ dislocations move parallel to the same (11) planes, a process which cannot

be explained by perfect glide. Indeed, the dislocation Burgers vector has a component normal to (11) planes, suggesting that the dislocation motion must be accompanied by some amount of climb.

The latter conclusion was verified by observations of the detailed core structure of the minority dislocations during their motion. As illustrated in Fig. 14, the number of sites (atomic density peaks) in the dislocation core is not conserved. In this particular example the core loses one site, whereas in other cases it could gain sites. As noted in Section 5, PFC simulations model an open system, in which the sites are not conserved locally or globally. The PFC simulations represent the material’s behavior at high temperatures approaching the melting point. Therefore, the continual creation, disappearance and redistribution of the sites can be interpreted as occurring by diffusion of vacancies. This interpretation can explain the motion of the minority dislocations along the majority slip planes by a combination of glide and climb. It should be emphasized that this mechanism was not, and could not be observed by the MD simulations because of the short time scale.

As mentioned earlier, the 2D character of the PFC methodology precludes a direction comparison of the structural units in high-angle GBs with their MD counterparts. Furthermore, the non-conservative nature of the PFC simulations often obscures unambiguous interpretation of atomic movements in complex GB structures. These complications prevented us from a more detailed PFC study of structural evolution and migration mechanisms of asymmetrical high-angle GBs.

8 Orientation and temperature dependencies of the driving stress

Previous MD simulations [26, 27] have shown that the resistance of symmetrical tilt GBs to coupled motion is relatively small and is due primarily to the stick-slip friction associated with nucleation of disconnection loops. The present MD simulations indicate that for asymmetric GBs, the resistance to motion is much greater and is caused by the need to avoid or overcome locked configurations between the dislocations gliding in intersecting slip planes. This resistance can be characterized by the average shear stress σ_{xy} required for sustaining a constant GB velocity.

Typical time dependencies of the shear stress are shown in Fig. 15 for an asymmetrical GB in Al. The initial rise of the stress is due to accumulation of elastic deformation until the stress reaches a level sufficient for sustaining the GB motion. The values of σ_{xy} reported below were

obtained by averaging over the steady state portion of the simulation run. At high temperatures the stress behavior is uniformly noisy, whereas low temperatures reveal multiple peaks characteristic of lock-unlock dynamics. It should be mentioned that in the case of perfectly regular stick-slip behavior, the average stress depends on the system size L_Y in the direction normal the GB plane [27]. However, the size-dependent correction to the stress decreases as $1/L_Y$ and for the large system sizes studied here is small.

The angle dependence of the average shear stress is plotted in Fig. 16 for a series of GBs with the same tilt angle $\theta = 16.26^\circ$ but varying inclination angle. Observe that the stress is highest for the “most asymmetrical” GBs with the inclination angles $|\phi| \approx 20^\circ$ - 30° . By contrast, the stresses required for moving the perfectly symmetrical GBs arising at $\phi = 0$ and $\pm 45^\circ$ are almost an order of magnitude smaller.

Fig. 16 demonstrates that the driving stress strongly decreases with temperature while preserving the same trend of the angle dependence. A more detailed temperature dependence of the stress is illustrated in Fig. 17 for an asymmetrical GB in Al. The rapid decrease of the stress with temperature reflects the thermally activated nature of the mechanisms responsible for the dislocation reactions, avoidance and unblocking. At high temperatures approaching the melting point, the driving stress is a factor of ten smaller than at room temperature.

9 Orientation and temperature dependencies of the coupling factor

For symmetrical GBs, the coupling factor depends on the tilt angle θ and temperature. As discussed in Section 3, previous MD simulations and experiments have revealed that β is a multi-valued function of θ and exhibits a discontinuous transition between two coupling modes. This transition was also confirmed in the present MD simulations (not shown here). The existence of two coupling modes and a discontinuity were also reproduced by the PFC simulations as illustrated in Fig. 18. The jump of the coupling factor occurs at an angle close to 20° for $\epsilon = 0.25$, which is the value of ϵ used in all the simulations of asymmetrical GBs, and close to 45° for $\epsilon = 0.05$. This difference reflects the ϵ -dependence of the PN barriers of the two types of dislocations as discussed earlier. Note the excellent agreement with predictions of the geometrical model of coupling [4], in which the two branches of the plot are described by Eqs. (4) and (5).

For asymmetrical GBs, we first discuss the $\theta = 16.26^\circ$ GBs which were studied in greatest detail. Fig. 19 reports the MD results for such boundaries in Cu and Al, showing two temperatures in each case. As indicated in Section 3, for θ below the critical angle of approximately

36° , β is expected to remain a positive constant equal to the ideal value given by Eq. (4). Instead, the simulations show that β of asymmetrical GBs varies with the inclination angle and, to a lesser degree, with temperature. The deviations from the ideal value of β are positive for some inclinations and negative for others. In Al the deviations can be as high as a factor of two. Al is dominated by positive deviations whereas in Cu both positive and negative deviations occur to nearly equal extent.

Similar results were obtained by PFC simulations (Fig. 20). In this case, the angle of discontinuity of symmetrical GBs is about 20° (Fig. 18), thus for $\theta = 16.26^\circ$ the coupling factor was again expected to remain constant. Instead, it varies with ϕ in a manner reminiscent of that in Al (cf. Fig. 19(b)). The deviations from the ideal β are always positive and reach a peak at about $\pm 30^\circ$. It should be emphasized that, despite the significant deviations of β from its ideal value in both MD and PFC simulations, the coupling factor remains positive. The positive sign of β indicates that the coupling mode remains the same at all inclination angles, which is consistent with our geometric analysis in Section 3.

Fig. 21(a) shows the MD results for high-angle GBs with $\theta = 36.87^\circ$. In this case, the coupling factor is expected to be negative at $\phi = 0$ and change sign to positive values as $|\phi|$ increases towards 45° (Section 3). This behavior is indeed confirmed by the simulations, despite the significant scatter of the points and deviations from the ideal values of β (Fig. 21(a)). The scatter strongly increases in the discontinuity regions, in which the magnitude of β becomes very large. Importantly, the PFC simulations reveal a very similar behavior of the coupling factor (Fig. 21(b)). The PFC plot is smoother than the MD plot and clearly reveals a “divergence” of β ($\beta \rightarrow \pm\infty$) in the narrow region where the sign changes.

Due to the high computational efficiency of the PFC method, it was possible to perform a large set of simulations with various misorientation and inclination angles. The results are summarized in Fig. 22 as a diagram in the coordinates θ - ϕ showing positive and negative values of β by different symbols. The boundary between the positive and negative regions has been drawn in this figure by hand and is intended to be a trend line. Despite the obvious scatter of the points, the shape of this line is in qualitative agreement with the geometric predictions shown in Fig. 2 as far as the overall shape of the two regions of positive and negative β is concerned. In particular, this diagram clearly shows that the discontinuity between the two coupling modes known from the previous work [2–4, 6, 15, 18–20] exists not only for symmetrical boundaries but also extends over the full range of inclination angles. However, sections of this diagram at a constant misorientation angle in the MD (Figs. 19 and 21(a)) and PFC (Figs. 20 and 21(b)) simulations clearly show that the magnitude of β is strongly dependent on inclination in a way that cannot be predicted by the geometrical considerations which were used to construct Fig. 2.

10 Discussion

The goal of this paper was to investigate the effect of the inclination angle on stress-driven motion of asymmetrical tilt GBs. To ensure generality of the results, the MD simulations were conducted over the full range of inclination angles, a wide temperature range, and in two different metals. Furthermore, the same GBs were also studied by PFC simulations, a recently developed methodology which provides access to atomic-level processes on diffusive time scales [32–45].

The MD and PFC methods are complementary to each other and their combination offers an efficient approach to multiscale problems such as GB motion. MD simulations are suitable for studying the effects of temperature, strain rate and stress on GB dynamics [26, 27] while simultaneously providing detailed information about atomic mechanisms. However, dislocation climb and other diffusion-controlled processes are beyond the time scale of MD simulations (tens of nanoseconds). The PFC approach is less quantitative and cannot be used for tracking all details of atomic movements. However, the material is modeled in the long-time regime in which atomic diffusion can readily occur. This gives access to GB migration mechanisms (such as dislocation climb) that would otherwise not be seen.

This study has shown that at a fixed misorientation angle θ , the coupling factor β varies with the inclination angle ϕ (Figs. 19, 20, 21). This observation does not confirm the geometric prediction [4] that β is a function of θ only. But there are other theoretical predictions that were tested and verified by this work. The most important of them is that most GBs in materials are coupled and, unless subject to imposed constraints, can be moved by applied stresses [4]. Indeed, the overwhelming majority of asymmetrical GBs tested here coupled to shear stresses and were moved by them. This finding clearly demonstrates that the coupling effect is *not* an attribute of only symmetrical GBs which were predominantly studied in previous work.

Furthermore, our simulations show that the two coupling modes found previously in [001] symmetrical tilt GBs [2–4, 6, 15, 18–20] continue to exist in asymmetrical GBs. The discontinuous transition between the modes also continues to exist for asymmetrical GBs as illustrated in Figs. 2 and 22. In the vicinity of the transition between the modes, the magnitude of the coupling factor becomes very large if not divergent (Fig. 21). In other words, a GB caught between the two coupling modes responds to applied shears by a processes which appears like sliding. Further investigations are needed to determine whether this response is a manifestation of a true sliding process or of the “dual behavior” with alternation between the two coupling modes as suggested on p. 4974 of [4].

The long-standing mystery [46] related to asymmetrical boundaries is how the dislocations gliding in intersecting slip planes avoid blocking each other (Fig. 7). Strong interactions between

such dislocations can explain the high stresses needed for the coupled motion of asymmetrical GBs (Fig. 16). At the same temperature and GB velocity, the shear stress required for steady-state motion of an asymmetrical GB can be an order of magnitude greater than for symmetrical boundaries. Several mechanisms have been found by which the dislocations alleviate the locks, most notably the dislocation reactions (Fig. 8) and dislocation avoidance (Figs. 9 and 10). When diffusion is allowed, the locks can also be overcome by dislocation climb as suggested by the PFC simulations (Section 7.2). The operation of these complex mechanisms responsible for the unlocking of the dislocations can explain the deviations of the coupling factor from the ideal geometrical value (Figs. 19, 20 and 21). Such deviations are predominantly positive, suggesting the existence of a sliding component along with coupling. However, a better understanding of the origin of the deviations requires further studies.

One might think that the deviations of the coupling factors from the ideal values could be caused by an additional driving force arising due to the elastic anisotropy of the lattice. For asymmetrical GBs, the elastic anisotropy creates a difference in elastic strain energies in the grains which may drive the GB motion. In fact, this driving force underlines one of the methods for studying GB migration by atomistic computer simulations, see e.g. [5] for review. However, because this driving force is quadratic in stress, large stresses need to be created in the grains in order to drive GB motion over a non-negligible distance. The stresses used in our study were smaller and unlikely to explain the above deviations. This is also evident from Fig. 17 showing the temperature dependencies of the coupling factor and stress. At temperatures above 500 K, β does not change within the scatter of the data points and remains higher than the ideal value. In the same temperature interval, the stress drops by about an order of magnitude, which rules out the possibility that the deviation from the ideal β was caused by additional GB motion induced by the stress.

It is interesting to compare the predictions of this modeling study with experimental data. Our main finding that most of asymmetrical GBs are moved by applied shear stresses is well consistent with experimental observations of stress-driven grain growth in nano-crystalline materials [16, 23, 24, 57]. Coupled motion of asymmetrical tilt GBs was also observed in experiments on bicrystalline samples subject to applied shear loads [6, 9]. In particular, Molodov et al. [6] studied stress-driven motion of [001] tilt GBs in Al bicrystals with different crystallographic parameters. One of the experiments was performed on a bicrystal with $\theta = 17.4^\circ$ and $\phi = 19.1^\circ$. The boundary was found to couple to the applied stress (see Figure 7 in [6]) and move with a coupling factor of 0.39, which is higher than the ideal geometrical value 0.31 computed from Eq. (4). To our knowledge, this is the only published value of coupling factor for an asymmetrical tilt GB in Al. This value can be *directly* compared with our simulations. Indeed, from the MD simulation

results for Al shown in Fig. 19(b), the boundary closest to the experimental conditions is one with $\theta = 16.26^\circ$ and $\phi = 18.44^\circ$. The computed coupling factor for this boundary is 0.40 at the temperature of 500 K and 0.38 at 900 K. Although the experimental temperature corresponding to $\beta = 0.39$ was not specified in [6], our prediction is in excellent agreement with experiment at both temperatures. Our simulations indicate that the overestimated coupling factor is caused by the dislocation reactions as discussed earlier in this paper. It should also be pointed out that the overestimated (relative to the geometric prediction) β value found in [6] is well consistent with the general trend found in this work by both MD (Fig. 19(b)) and PFC (Fig. 20) simulations.

The symmetry analysis (Sections 2 and 3) and the simulations reported in this paper provide a theoretical basis for designing future experiments. In particular, for [001] tilt GBs in FCC metals, the following experiments would provide the most direct test of our theoretical predictions. First, for a given material, a series of symmetrical tilt GBs should be studied over the entire range of misorientation to determine the critical switching angle θ_c between the different coupling modes $\langle 100 \rangle$ and $\langle 110 \rangle$. This series of experiments would parallel the experimental study of symmetric tilt GBs in Al where θ_c was estimated to be between 30.5° and 36.5° [19]. After this critical angle has been established, the following series of experiments should be able to reveal the three distinct regimes predicted in this paper:

1. Measurements of β at a fixed tilt angle $\theta < \theta_c$ and varying inclination angle ϕ . The coupling factor is expected to remain positive but may deviate from the value predicted by Eq. (4) (most probably in the positive direction).
2. Measurements of β at a fixed tilt angle $\theta > (90^\circ - \theta_c)$ and varying inclination angle ϕ . The coupling factor is expected to remain native but may deviate from the value predicted by Eq. (5) (most probably in the negative direction).
3. Measurements of β at a fixed tilt angle $\theta_c < \theta < (90^\circ - \theta_c)$ and varying inclination angle ϕ . The coupling factor is expected to switch from positive at small ϕ to negative as ϕ approaches $\pm 45^\circ$. At angles close to the sign change, the boundary may exhibit a sliding-like behavior.

It is important to emphasize that the critical switching angle between the two coupling modes is essential in determining the range of misorientation, $\theta_c < \theta < (90^\circ - \theta_c)$, which is predicted to exhibit the most interesting and novel dependence of the coupling on inclination. As indicated earlier, the specific critical angle of $\theta_c = 36^\circ$ mentioned above refer to EAM Cu and can be different for other metals.

11 Conclusions

In conclusions, we have shown by computer simulations that the coupling effect exists for the vast majority of symmetrical as well as asymmetrical tilt GBs. Furthermore, as for symmetrical GBs, the coupling of asymmetrical boundaries can occur in multiple models with coupling factors β that can have different signs. The magnitude of β is generally strongly dependent on the inclination angle in a way that cannot be fully predicted from purely geometrical considerations. The most dramatic manifestation of this dependence is the sharp increase in the magnitude of β in a range of angles near the boundary between regions of opposite signs of β . This confers GBs with a sliding-like behavior that could potentially have a strong influence on mechanical properties of polycrystalline materials.

Furthermore, we have found that the motion of asymmetrical GBs can be mediated by several different processes. In the MD simulations where vacancy diffusion was negligible, the motion of GB dislocations on different slip planes was accommodated by dislocation reactions and/or avoidance. In contrast, in the PFC simulations which incorporate diffusive processes generally occurring at high temperatures, dislocation climb facilitated collective motion of dislocations with different Burgers vectors, allowing the GB to avoid locks and move smoothly.

Importantly, the dependence of the coupling factor β on GB bicrystallography was found to be strikingly similar in the MD and PFC simulations, despite the mentioned differences in the atomistic details of GB migration. Both simulation methods predict similar shapes of the regions of opposite signs of β in the parameter space of angles. These shapes are consistent with considerations of crystal symmetry and the different PN barriers of the dislocations moving in different slip planes. Both methods predict diverging magnitudes of β near the boundary separating the regions of positive and negative values of β . We therefore expect these basic features of asymmetrical GBs to pertain to a wide range of materials, temperatures and other physical conditions.

Finally, our simulation results are in encouraging agreement with experiments on stress-driven GB motion in polycrystalline materials and bicrystalline samples. Furthermore, they are in excellent agreement with the recently measured experimental value of the coupling factor for an asymmetrical tilt GB in an Al bicrystal [6]. When discussing the problem of coupled motion of asymmetrical boundaries, Molodov et al. [6] remark: “Further investigations, especially molecular dynamics simulations are obviously needed to clarify the mechanisms of this phenomenon, specific atomic rearrangements, dislocation processes, and reactions involved in the process of boundary migration.” We hope that the present study has made a step in this direction and will motivate further experiments.

Acknowledgments - This work was supported by the U.S. Department of Energy, the Physical Behavior of Materials Program, through Grants No. DE-FG02-01ER45871 (ZTT and YM) and DE-FG02-07ER46400 (AA and AK).

References

- [1] J. W. Cahn and J. E. Taylor. A unified approach to motion of grain boundaries, relative tangential translation along grain boundaries, and grain rotation. *Acta Mater.*, 52:4887–4998, 2004.
- [2] A. Suzuki and Y. Mishin. Atomic mechanisms of grain boundary motion. *Mater. Sci. Forum*, 502:157–162, 2005.
- [3] J. W. Cahn, Y. Mishin, and A. Suzuki. Duality of dislocation content of grain boundaries. *Philos. Mag.*, 86:3965–3980, 2006.
- [4] J. W. Cahn, Y. Mishin, and A. Suzuki. Coupling grain boundary motion to shear deformation. *Acta Mater.*, 54:4953–4975, 2006.
- [5] Y. Mishin, M. Asta, and Ju Li. Atomistic modeling of interfaces and their impact on microstructure and properties. *Acta Mater.*, 58:1117 – 1151, 2010.
- [6] D. A. Molodov, T. Gorkaya, and G. Gottstein. Dynamics of grain boundaries under applied mechanical stress. *J. Mater. Sci.*, 46:4318–4326, 2011.
- [7] T. Gorkaya, K. D. Molodov, D. A. Molodov, and G. Gottstein. Concurrent grain boundary motion and grain rotation under an applied stress. *Acta Mater.*, 59:5674–5680, 2011.
- [8] D. A. Molodov, T. Gorkaya, and G. Gottstein. Migration of the $\sigma 7$ tilt grain boundary in al under an applied external stress. *Scripta Mater.*, 65:990–993, 2011.
- [9] B. Syed, D. Catoor, R. Mishra, and K.S. Kumar. Coupled motion of $[10 - 10]$ tilt boundaries in magnesium bicrystals. *Philosophical Magazine*, 92(12):1499–1522, 2012.
- [10] C. H. Li, E. H. Edwards, J. Washburn, and J. Parker. Stress-induced movement of crystal boundaries. *Acta Metall.*, 1:223, 1953.
- [11] D. W. Bainbridge, C. H. Li, and E. H. Edwards. Recent observations on the motion of small angle dislocation boundaries. *Acta Metall.*, 2:322–333, 1954.

- [12] M. Winning, G. Gottstein, and L. S. Shvindlerman. Stress induced grain boundary motion. *Acta Mater.*, 49:211–219, 2001.
- [13] M. Winning, G. Gottstein, and L. S. Shvindlerman. On the mechanisms of grain boundary migration. *Acta Mater.*, 50:353–363, 2002.
- [14] H. Yoshida, K. Yokoyama, N. Shibata, Y. Ikuhara, and T. Sakuma. High-temperature grain boundary sliding behavior and grain boundary energy in cubic zirconia bicrystals. *Acta Mater.*, 52:2349–2357, 2004.
- [15] D.A. Molodov, T. Gorkaya, and G. Gottstein. Mechanically driven migration of $\langle 100 \rangle$ tilt grain boundaries in Al-bicrystals. *Materials Science Forum*, 558-559:927–932, 2007.
- [16] M. Legros, D. S. Gianola, and K. J. Hemker. In situ TEM observations of fast grain-boundary motion in stressed nanocrystalline aluminum films. *Acta Mater.*, 56:3380–3393, 2008.
- [17] F. Momprou, D. Caillard, and M. Legros. Grain boundary shear-migration coupling. i. in situ TEM straining experiments in Al polycrystals. *Acta Mater.*, 57:2198–2209, 2009.
- [18] D. A. Molodov and L. S. Shvindlerman. Interface migration in metals (Al): "vingt ans apres" (twenty years later). *Int. J. Mater. Res.*, 100:461–482, 2009.
- [19] T. Gorkaya, D. A. Molodov, and G. Gottstein. Stress-driven migration of symmetrical $\langle 100 \rangle$ tilt grain boundaries in Al bicrystals. *Acta Mater.*, 57:5396–5405, 2009.
- [20] T. Gorkaya, T. Berlet, D. A. Molodov, and G. Gottstein. Experimental method for true in situ measurements of shear-coupled grain boundary migration. *Scripta Mater.*, 63:633–636, 2010.
- [21] J. Monk, B. Hyde, and D. Farkas. The role of partial grain boundary dislocations in grain boundary sliding and coupled grain boundary motion. *J. Mater. Sci.*, 41:7741–7746, 2006.
- [22] T. Zhu, J. Li, A. Samanta, H. G. Kim, and S. Suresh. Interfacial plasticity governs strain rate sensitivity and ductility in nanostructured materials. *Proc. Nat. Acad. Sci. USA*, 104:3031–3036, 2007.
- [23] K. J. Hemker and W. N. Sharpe. Microscale characterization of mechanical properties. *Annu. Rev. Mater. Res.*, 37:93–126, 2007.
- [24] D. S. Gianola, C. Eberl, X. M. Cheng, and K. J. Hemker. Stress-driven surface topography evolution in nanocrystalline Al thin films. *Advanced Materials*, 20:303–308, 2008.

- [25] J. W. Cahn and Y. Mishin. Recrystallization initiated by low-temperature grain boundary motion coupled to stress. *Int. J. Mater. Res.*, 100:510–515, 2009.
- [26] Y. Mishin, A. Suzuki, B. Uberuaga, and A. F. Voter. Stick-slip behavior of grain boundaries studied by accelerated molecular dynamics. *Phys. Rev. B*, 75:224101, 2007.
- [27] V. A. Ivanov and Y. Mishin. Dynamics of grain boundary motion coupled to shear deformation: An analytical model and its verification by molecular dynamics. *Phys. Rev. B*, 78:064106, 2008.
- [28] Z. T. Traut and Y. Mishin. Grain boundary migration and grain rotation studied by molecular dynamics. *Acta Mater.*, 60:2407–2424, 2012.
- [29] A. Elsener, O. Politano, P. M. Derlet, and H. Van Swygenhoven. Variable-charge method applied to study coupled grain boundary migration in the presence of oxygen. *Acta Mater.*, 57:1988–2001, 2009.
- [30] L. A. Wan and S. Q. Wang. Shear response of the sigma 11, <110> (131) symmetric tilt grain boundary in fcc metals studied by molecular dynamics. *Model. Simul. Mater. Sci. Eng.*, 17:045008, 2009.
- [31] H. Zhang, D. Du, and D. J. Srolovitz. Effect of boundary inclination and boundary type on shear-driven grain boundary migration. *Philos. Mag.*, 88:243–256, 2008.
- [32] K. R. Elder, K. Katakowski, M. Haataja, and M. Grant. Modeling elasticity in crystal growth. *Phys. Rev. Lett.*, 88:245701, 2002.
- [33] K. R. Elder and M. Grant. Modeling elastic and plastic deformations in non equilibrium processing using phase field crystals. *Phys. Rev. E*, 70:051605, 2004.
- [34] J. Berry, M. Grant, and K. R. Elder. Diffusive atomistic dynamics of edge dislocations in two dimensions. *Phys. Rev. E*, 73:031609, 2006.
- [35] P. Stefanovic, M. Haataja, and N. Provatas. Phase-field crystals with elastic interactions. *Phys. Rev. Lett.*, 96:225504, 2006.
- [36] K. A. Wu and A. Karma. Phase-field crystal modeling of equilibrium bcc-liquid interfaces. *Phys. Rev. B*, 76:184107, 2007.
- [37] K. R. Elder, N. Provatas, J. Berry, P. Stefanovic, and M. Grant. Phase-field crystal modeling and classical density functional theory of freezing. *Phys. Rev. B*, 75:064107, 2007.

- [38] J. Berry, K. R. Elder, and M. Grant. Melting at dislocations and grain boundaries: A phase field crystal study. *Phys. Rev. B*, 77:224114, 2008.
- [39] J. Mellenthin, A. Karma, and M. Plapp. Phase-field crystal study of grain-boundary pre-melting. *Phys. Rev. B*, 78:184110, 2008.
- [40] P. Stefanovic, M. Haataja, and N. Provatas. Phase field crystal study of deformation and plasticity in nanocrystalline materials. *Phys. Rev. E*, 80:046107, 2009.
- [41] K. A. Wu, A. Adland, and A. Karma. Phase-field-crystal model for fcc ordering. *Phys. Rev. E*, 81:061601, 2010.
- [42] A. Jaatinen, C. V. Achim, K. R. Elder, and T. Ala-Nissila. Phase field crystal study of symmetric tilt grain boundaries of iron. *Tech. Mech.*, 30:169–176, 2010.
- [43] R. Spatschek and A. Karma. Amplitude equations for polycrystalline materials with interaction between composition and stress. *Phys. Rev. B*, 81:214201, 2010.
- [44] D. L. Olmsted, D. Buta, A. Adland, S. M. Foiles, M. Asta, and A. Karma. Dislocation-pairing transitions in hot grain boundaries. *Phys. Rev. Lett.*, 106:046101, 2011.
- [45] A. Adland, R. Spatschek, D. Buta, M. Asta, and A. Karma. Phase-field-crystal study of grain-boundary premelting and shearing for bcc ordering (preprint, 2012). 2012.
- [46] W. T. Read and W. Shockley. Dislocation models of crystal grain boundaries. *Phys. Rev.*, 78:275–289, 1950.
- [47] J. E. Taylor and J. W. Cahn. Shape accommodation of a rotating embedded crystal via a new variational formulation. *Interfaces and Free Boundaries*, 9:493–512, 2007.
- [48] H. Zhang. Atomistic simulation of sliding of [1010] tilt grain boundaries in mg. *J. Mater. Res.*, 24:3446–3453, 2009.
- [49] P. Y. Chan, N. Goldenfeld, and J. Dantzig. Molecular dynamics on diffusive time scales from the phase-field-crystal equation. *Phys. Rev. E*, 79:035701R, 2009.
- [50] A. P. Sutton and R. W. Balluffi. *Interfaces in Crystalline Materials*. Clarendon Press, Oxford, 1995.
- [51] Y. Mishin, M. J. Mehl, D. A. Papaconstantopoulos, A. F. Voter, and J. D. Kress. Structural stability and lattice defects in copper: Ab initio, tight-binding and embedded-atom calculations. *Phys. Rev. B*, 63:224106, 2001.

- [52] Y. Mishin, D. Farkas, M. J. Mehl, and D. A. Papaconstantopoulos. Interatomic potentials for monoatomic metals from experimental data and ab initio calculations. *Phys. Rev. B*, 59:3393–3407, 1999.
- [53] A. Suzuki and Y. Mishin. Atomistic modeling of point defects and diffusion in copper grain boundaries. *Interface Science*, 11:131–148, 2003.
- [54] G. J. Tucker, J. A. Zimmerman, and D. L. McDowell. Shear deformation kinematics of bicrystalline grain boundaries in atomistic simulations. *Model. Simul. Mater. Sci. Eng.*, 18:015002, 2010.
- [55] A. Adland and A. Karma. Phase-field crystal dynamics for solids (preprint, 2012). 2012.
- [56] M. Klement and J. Friedel. Disclinations, dislocations, and continuous defects: A reappraisal. *Rev. Mod. Phys.*, 80:61–115, 2008.
- [57] K. Zhang, J. R. Weertman, and J. A. Eastman. Rapid stress-driven grain coarsening in nanocrystalline Cu at ambient and cryogenic temperatures. *Appl. Phys. Lett.*, 87:061921, 2005.

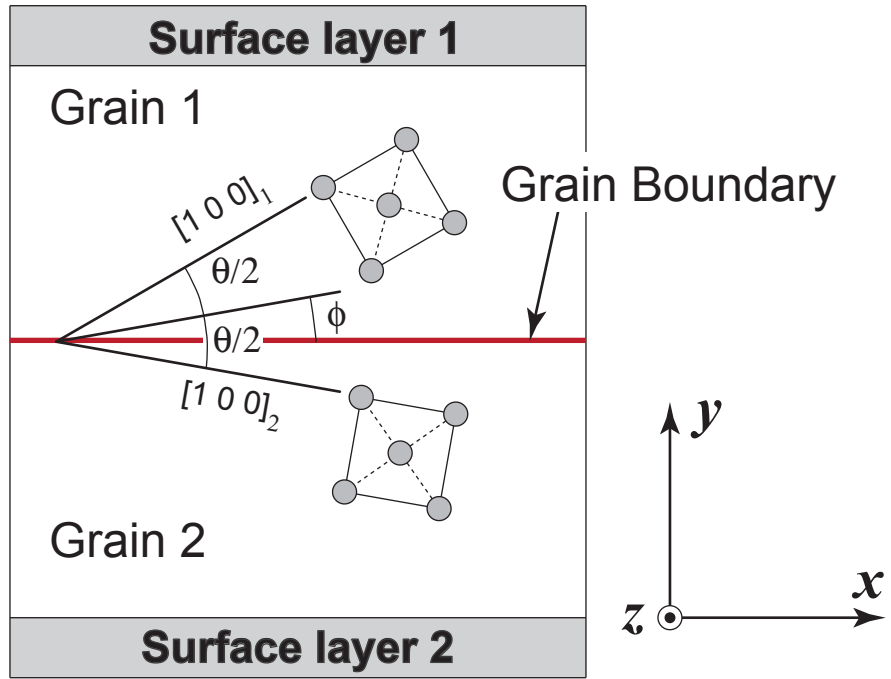


Figure 1: Geometry of the MD simulation block employed in this study.

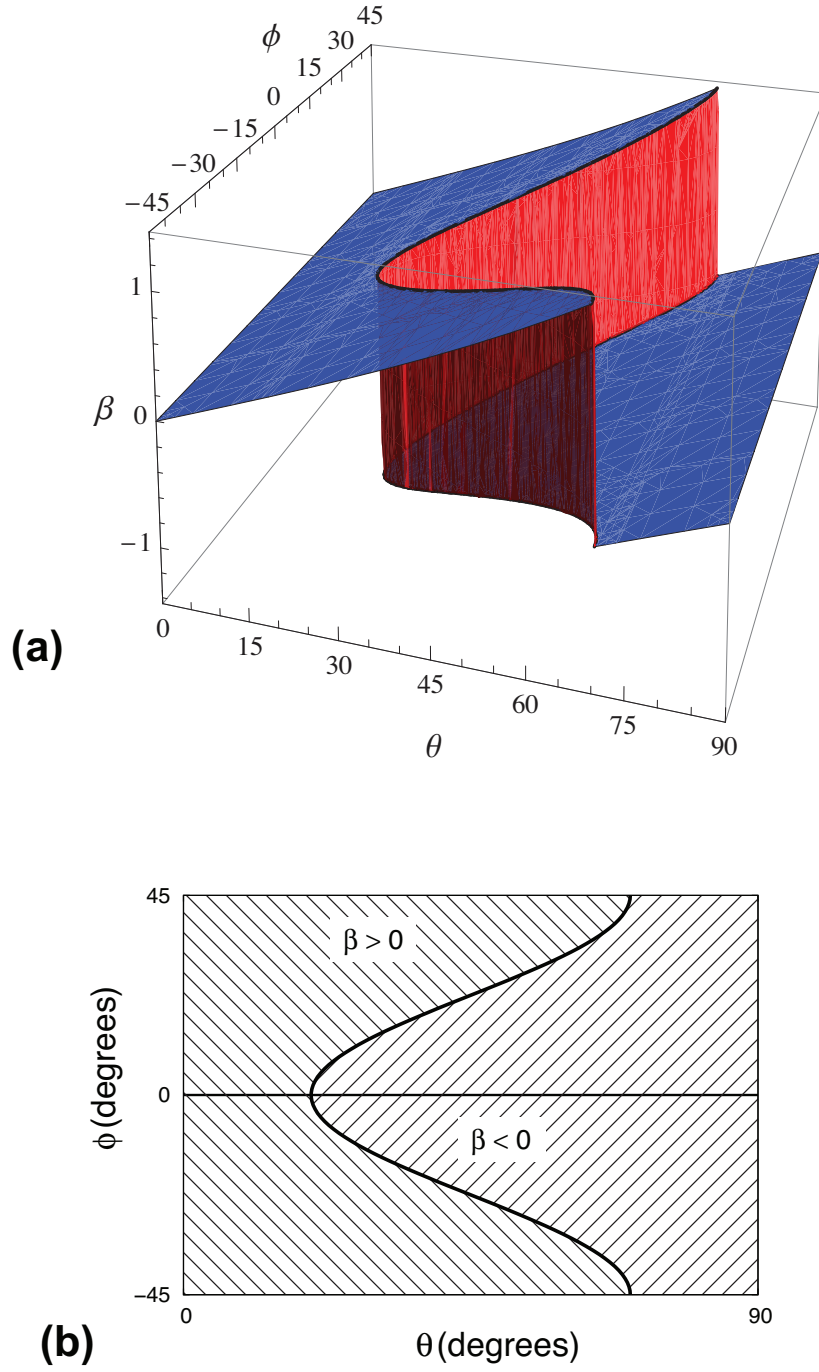


Figure 2: Schematic dependence of the coupling factor β on the tilt angle θ and the inclination angle ϕ . (a) Surface plot with two sheets representing the $\langle 100 \rangle$ and $\langle 110 \rangle$ modes of coupling. The coupling factor is discontinuous along the cut. (b) Projection of the surfaces on the θ - ϕ plane, showing the areas of positive and negative values of β .

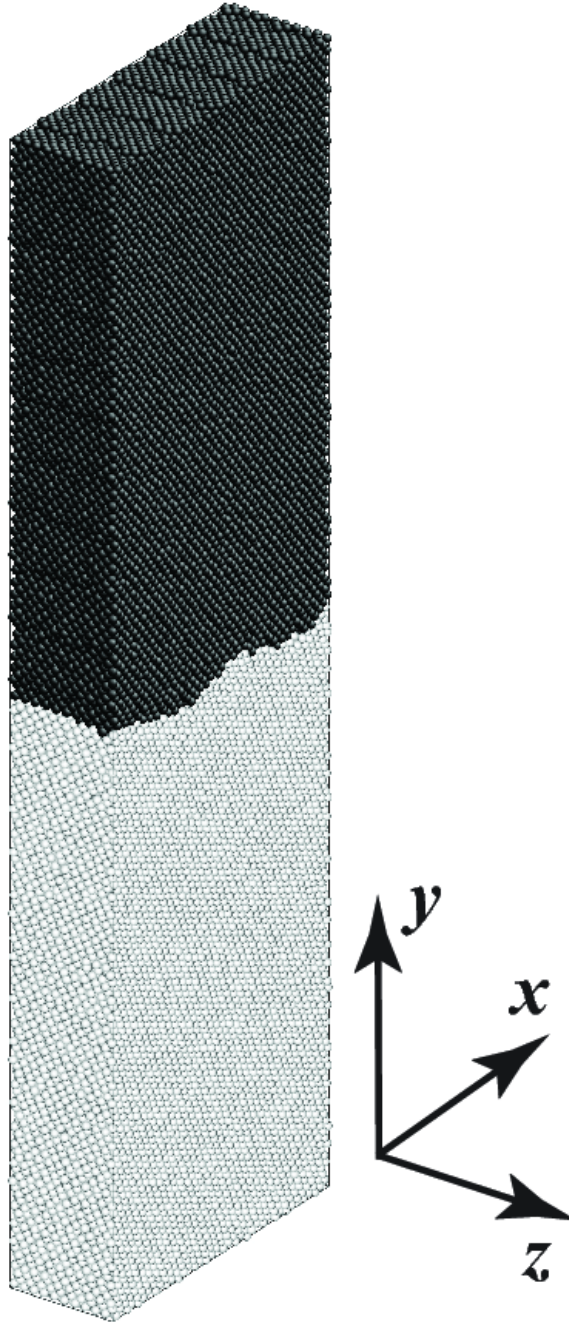


Figure 3: Illustration of partitioning of atoms between the two grains using the orientation parameter method. The image was taken from MD simulations of the Cu GB with $\theta = 16.26^\circ$ and $\phi = 14.04^\circ$ at 500 K. The bright and dark colors designate atoms assigned to different grains.

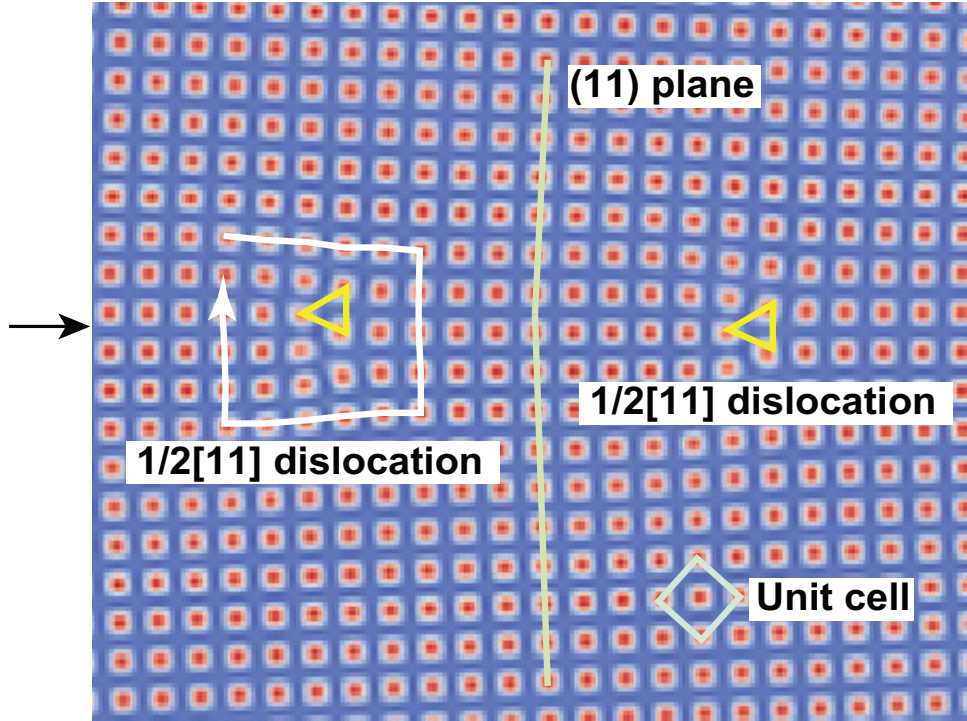


Figure 4: PFC simulated structure of the symmetrical tilt GB with $\theta = 80^\circ$. The GB plane is horizontal and its approximate position is indicated by an arrow. The structure is composed of $1/2\langle 11 \rangle$ dislocations whose cores are marked by yellow triangles. A Burgers circuit drawn around one of the dislocations is shown in white color. The unit cell of the 2D lattice and a perfect (11) crystal plane passing between the dislocations are indicated.

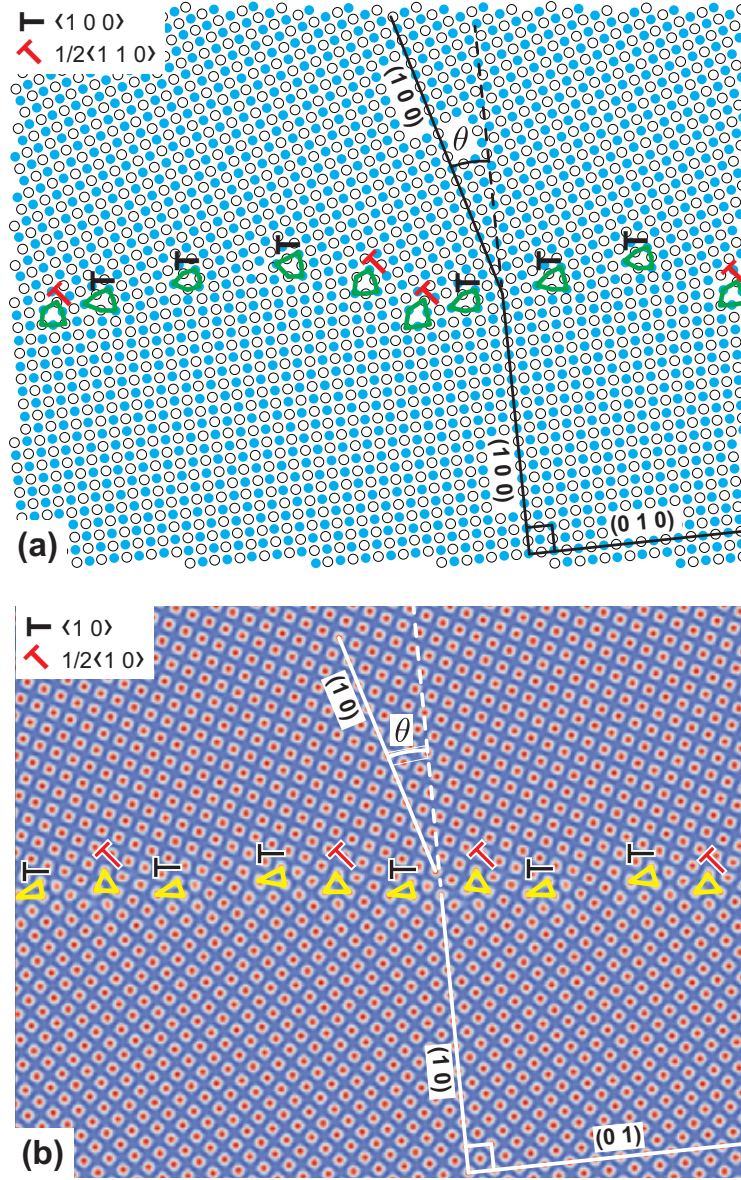


Figure 5: Equilibrium structure of the asymmetrical GB with $\theta = 16.26^\circ$ and $\phi = 14.04^\circ$. (a) Obtained by MD simulations of Cu and Al. The open and filled circles mark atomic positions in alternate (002) planes. The structural units forming the dislocation cores are outlined. (b) Obtained by PFC simulations. The dislocation cores are marked by yellow triangles. Both structures are composed of six $\langle 100 \rangle$ dislocations and four $1/2\langle 110 \rangle$ dislocations in each structural period.

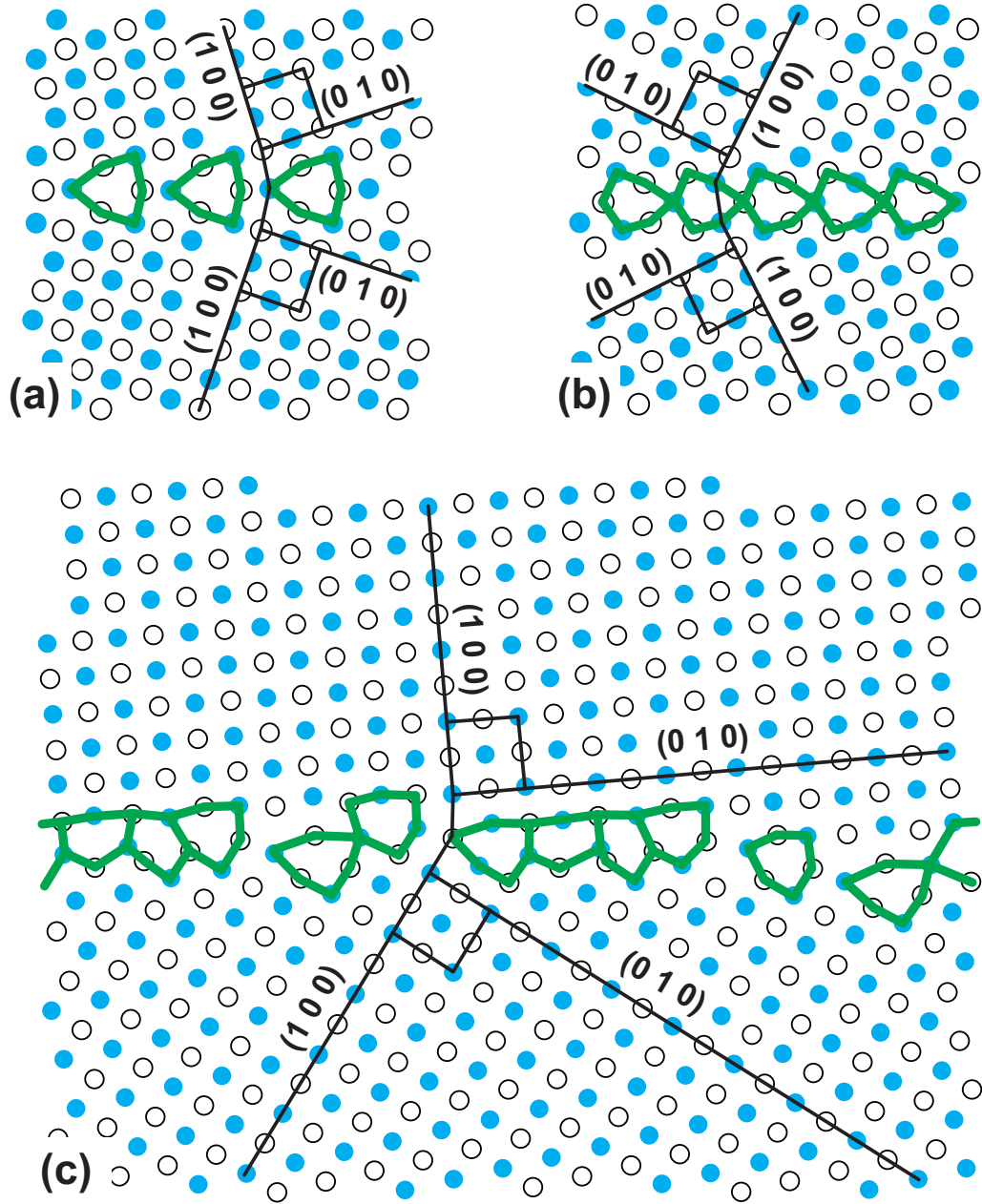


Figure 6: Examples of equilibrium structures of $\Sigma 5$ GBs ($\theta = 36.87^\circ$) obtained by MD simulations of Cu and Al. (a) Symmetrical (310) boundary with $\phi = 0$. (b) Symmetrical (210) boundary with $\phi = 45^\circ$. (c) Asymmetrical boundary with $\phi = 14.04^\circ$. The kite-shape structural units of the GB structures are outlined. Selected crystal planes are labeled for clarity.

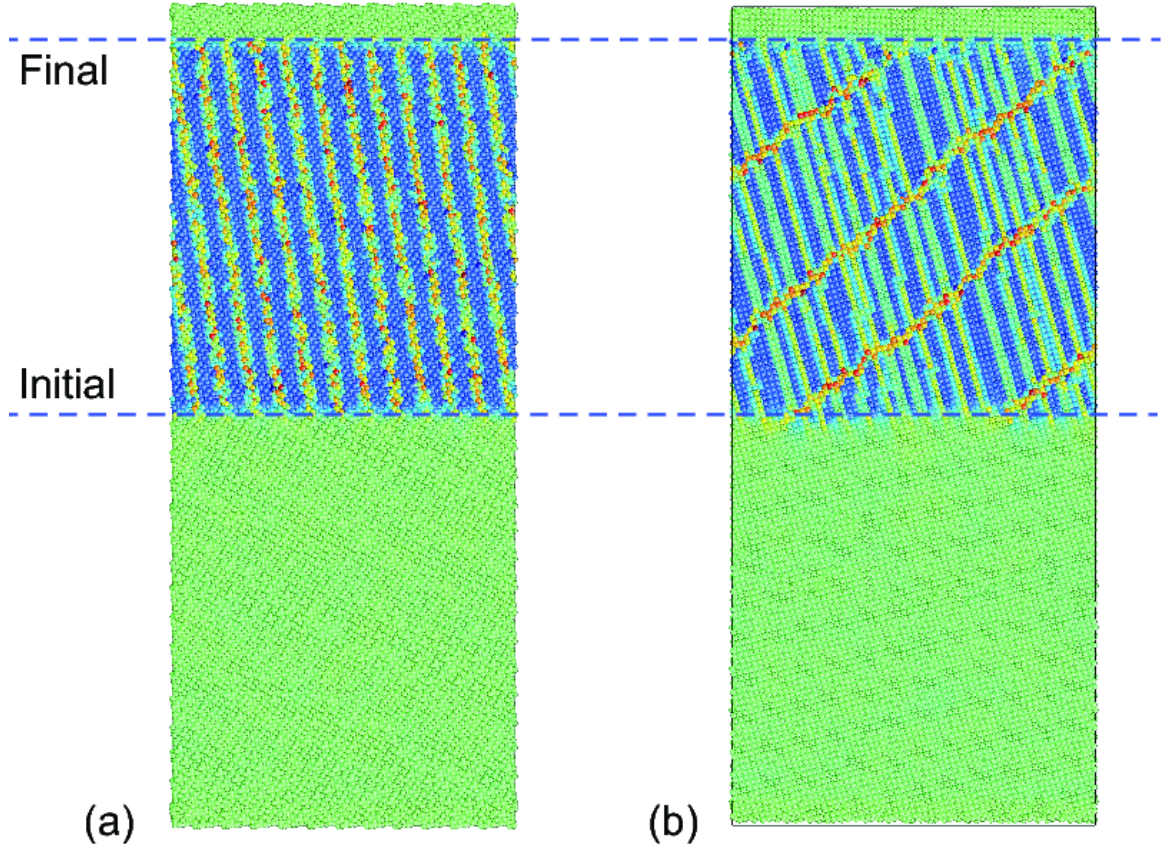


Figure 7: Traces of gliding dislocations in MD simulations of coupled GB motion in Cu at 500 K. The dislocation traces are revealed using the micro-rotation vector method from [54]. The green and blue colors represent different localized lattice deformations. The initial and final GB positions are indicated. (a) Symmetrical tilt GB with $\theta = 16.26^\circ$ and $\phi = 0$ moves by collective glide of $\langle 100 \rangle$ dislocations. (b) Asymmetrical tilt GB with $\theta = 16.26^\circ$ and $\phi = 38.06^\circ$ moves by collective glide and reactions of $\langle 100 \rangle$ (minority) and $1/2\langle 110 \rangle$ (majority) dislocations.

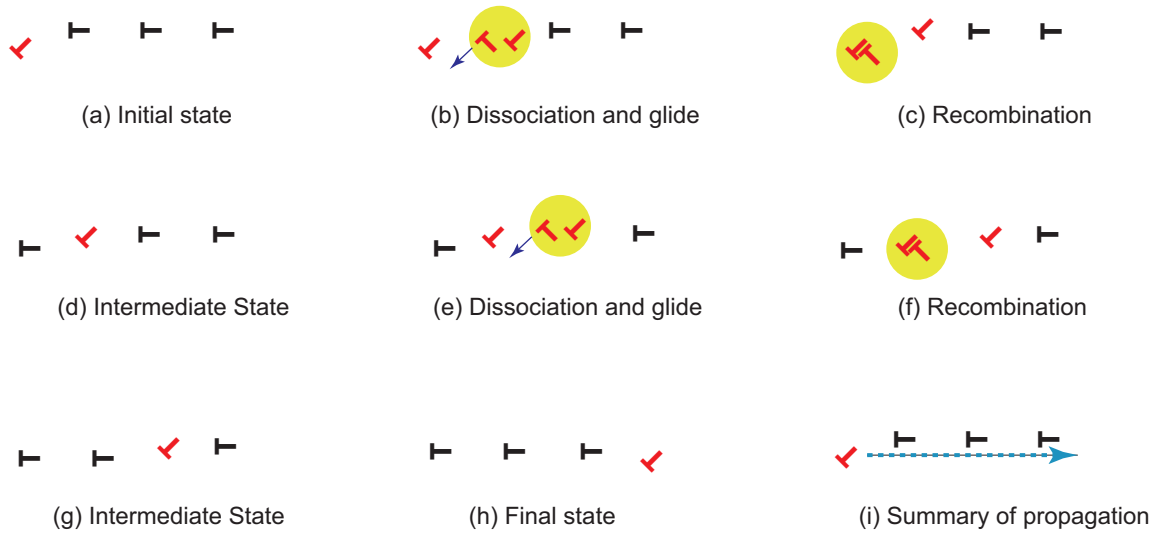


Figure 8: Schematic of dislocation propagation along a GB by a chain of dislocation reactions. The dislocation notation is the same as in Figure 5. The dislocation pairs undergoing dissociation and recombination reactions are encircled. (a) Initial state. (d) and (g) Intermediate states. (h) Final state. (i) Summary of the whole process.

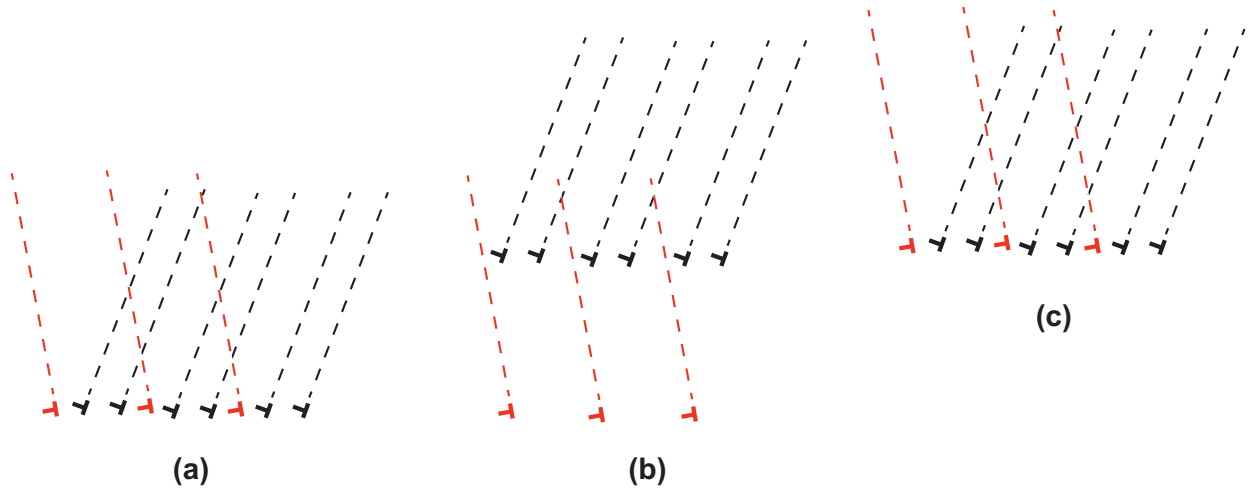


Figure 9: Schematic illustration of the dislocation avoidance mechanism for an asymmetrical GB moving upward. The dislocation notation is the same as in Figure 5. (a) Initial dislocation structure comprising $\langle 100 \rangle$ (majority) and $1/2\langle 110 \rangle$ (minority) dislocations. The dashed lines indicate the dislocation slip planes ahead of their motion. (b) The majority dislocations move forward while the minority are left behind, creating gaps in the GB structure. (c) When the gaps are aligned with the slip planes of the minority dislocations, the latter move forward and fill the gaps, recreating the initial GB structure in a new position.

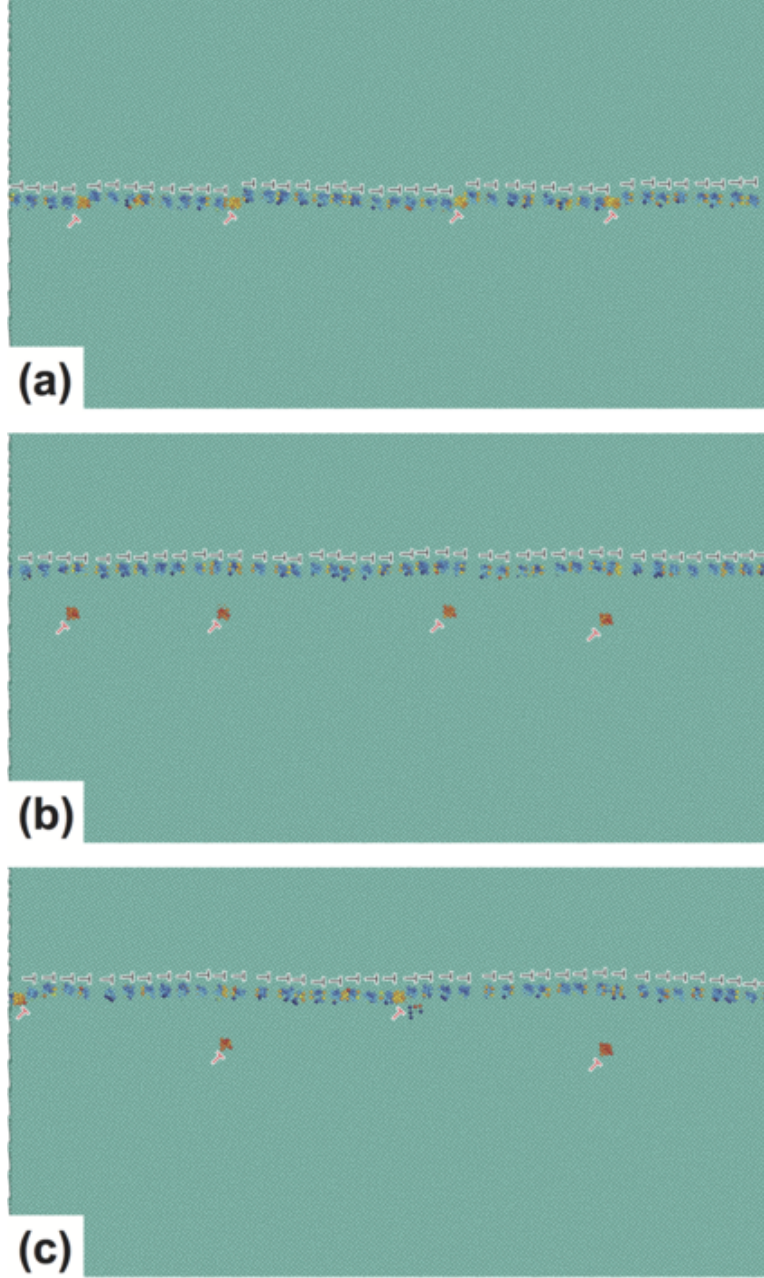


Figure 10: MD snapshots illustrating the dislocation avoidance mechanism for an asymmetrical GB in Cu with $\theta = 16.26^\circ$ and $\phi = 2.73^\circ$. The GB moves upward. (a) Initial GB structure. (b) The minority dislocations $1/2\langle 110 \rangle$ are left behind creating gaps between the majority dislocations $\langle 100 \rangle$. (c) When proper alignment is reached, two of the minority dislocations catch up with the boundary and fill the gaps. The remaining minority dislocations subsequently fill other gaps (not shown). The dislocations are visualized by constructing small Burgers loops around their cores and color-coding a selected projection of the closure failure. The simulation temperature is 500 K.

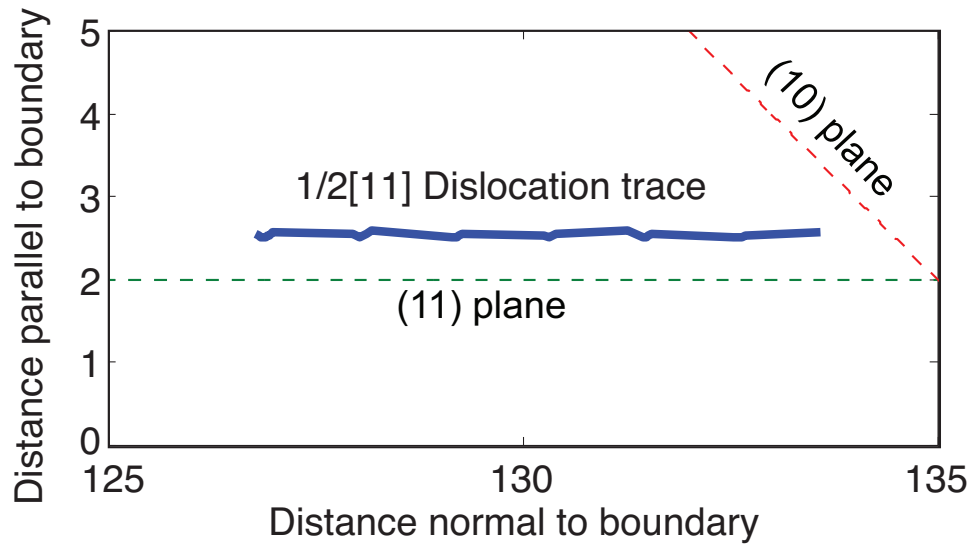


Figure 11: A typical trace of a $1/2\langle 11 \rangle$ dislocation in PFC simulations of coupled motion of the symmetrical GB with $\theta = 16.26^\circ$ and $\phi = 45^\circ$. The dashed lines indicate (11) and (10) crystal planes in the advancing grain. The dislocation moves parallel to (11) planes consistent with the glide mechanism. The distances are in Angstroms.

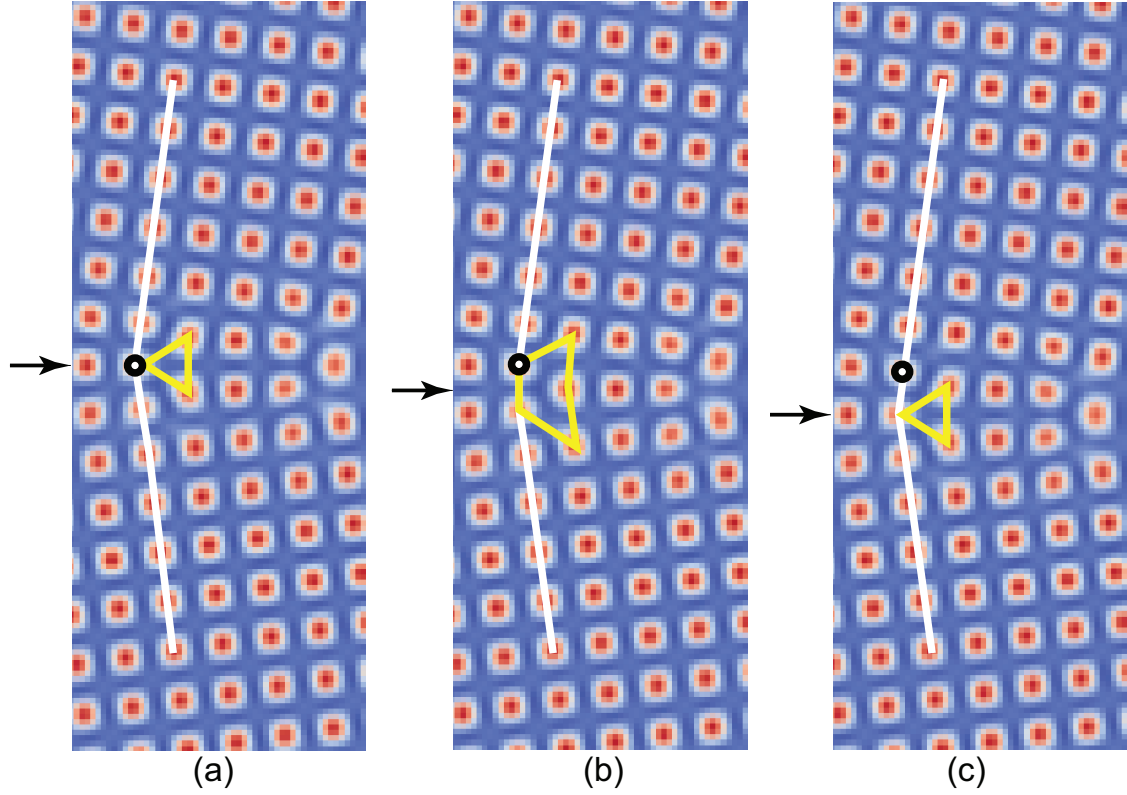


Figure 12: PFC observation of $1/2\langle 11 \rangle$ dislocation glide during coupled motion of the symmetrical GB with $\theta = 16.26^\circ$ and $\phi = 45^\circ$. Frames (a), (b) and (c) show sequential configurations of the boundary moving down, with the current GB position shown by an arrow. The dislocation core is marked by a yellow triangle. The white line connects a selected set of sites (the same in all three frames) located in a (11) plane. One of the sites is labeled by an open circle for tracking.

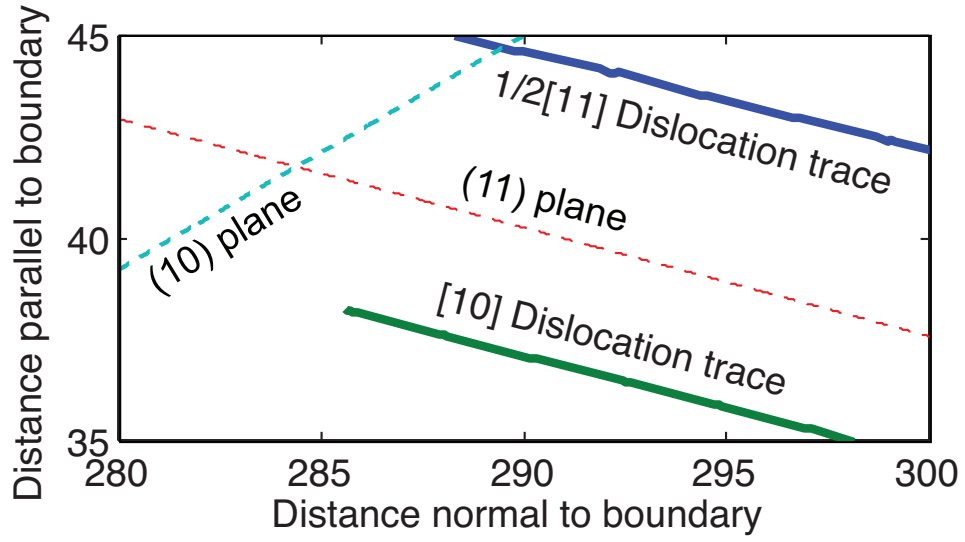


Figure 13: Typical dislocation traces in PFC simulations of coupled motion of an asymmetrical GB with $\theta = 16.26^\circ$ and $\phi = 30.3^\circ$. The dashed lines indicate (11) and (10) crystal planes in the advancing grain. Both $\langle 10 \rangle$ and $1/2\langle 11 \rangle$ dislocations move parallel to (11) planes, suggesting that the motion of $\langle 10 \rangle$ dislocations involves climb. The distances are in Angstroms.

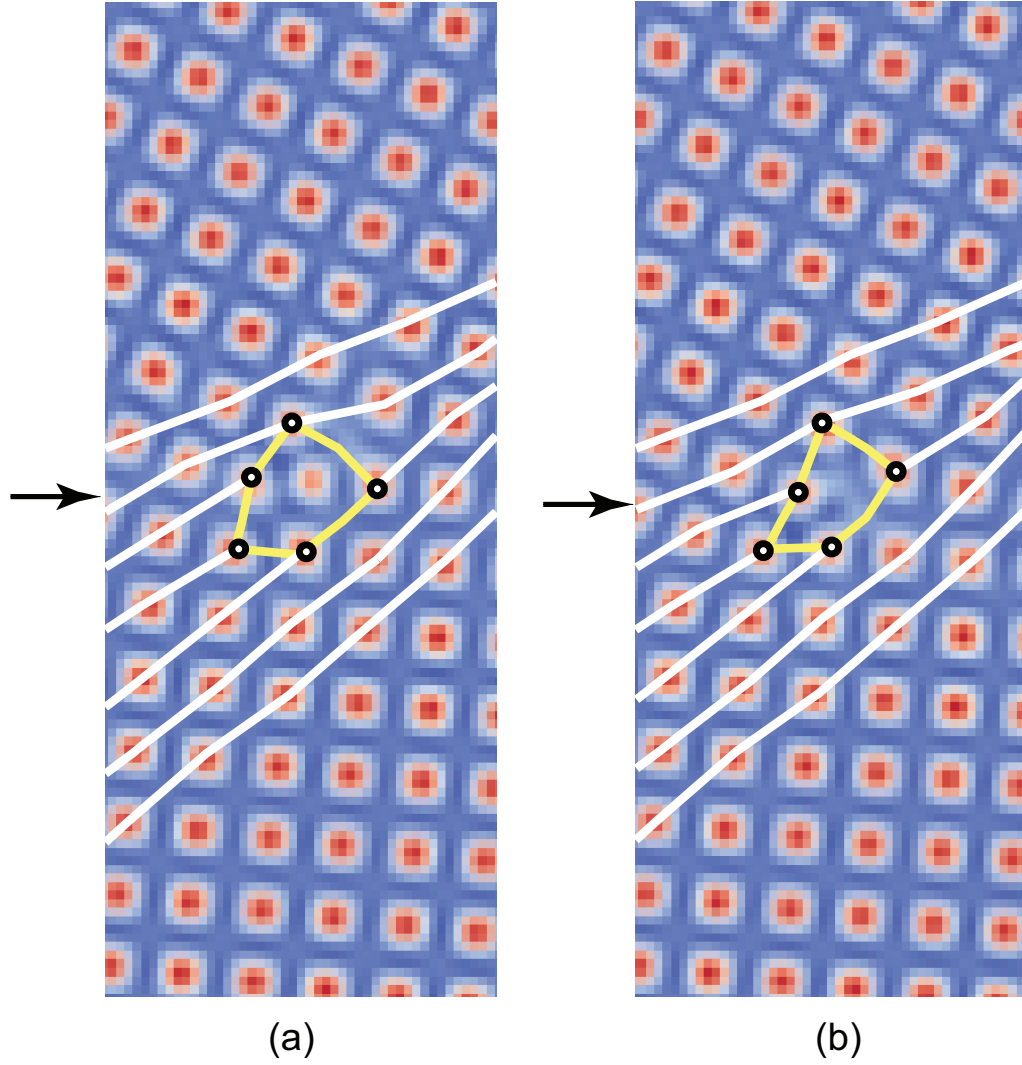


Figure 14: PFC observation of $\langle 10 \rangle$ dislocation motion during coupled migration of an asymmetrical GB with $\theta = 16.26^\circ$ and $\phi = 30.3^\circ$. Frames (a) and (b) show sequential configurations of the boundary moving down, with the current GB position shown by an arrow. The dislocation core region is outlined by five selected sites marked by open circles and connected by yellow lines. In (a), the yellow polygon encircles a sixth site, whereas in (b) this site disappears, providing evidence of dislocation climb. The white lines outline some of the (20) planes as a guide to the eye.

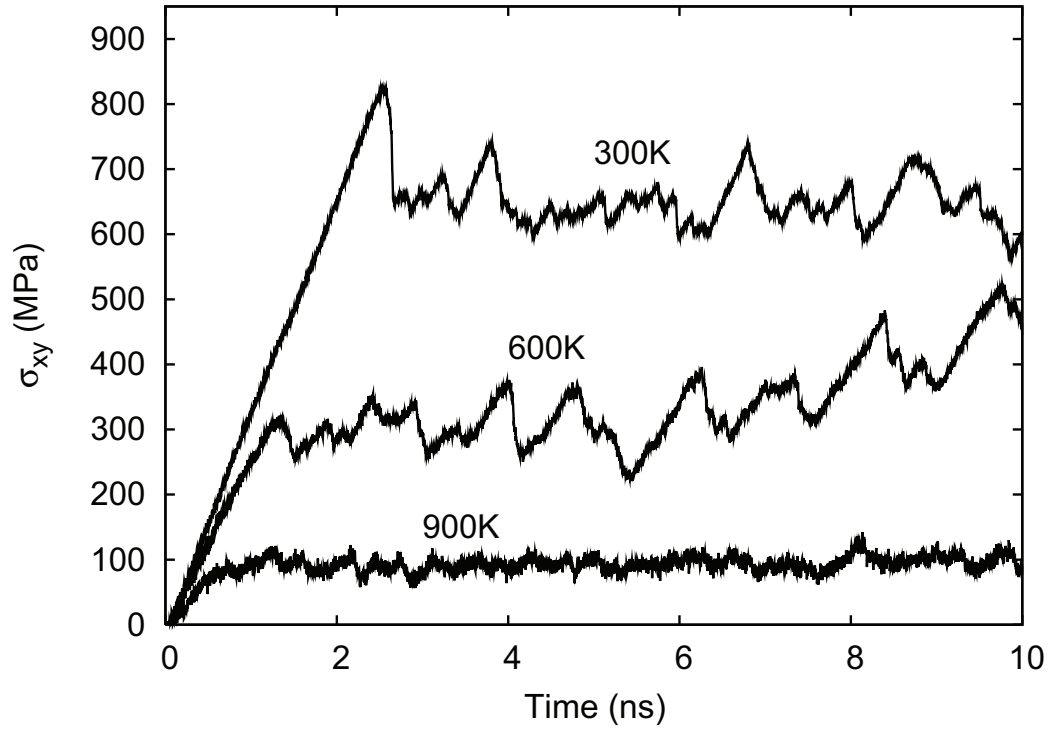


Figure 15: Typical time dependencies of the shear stress during coupled motion of an asymmetrical GB in Al with $\theta = 16.26^\circ$ and $\phi = -18.44^\circ$ at three different temperatures.

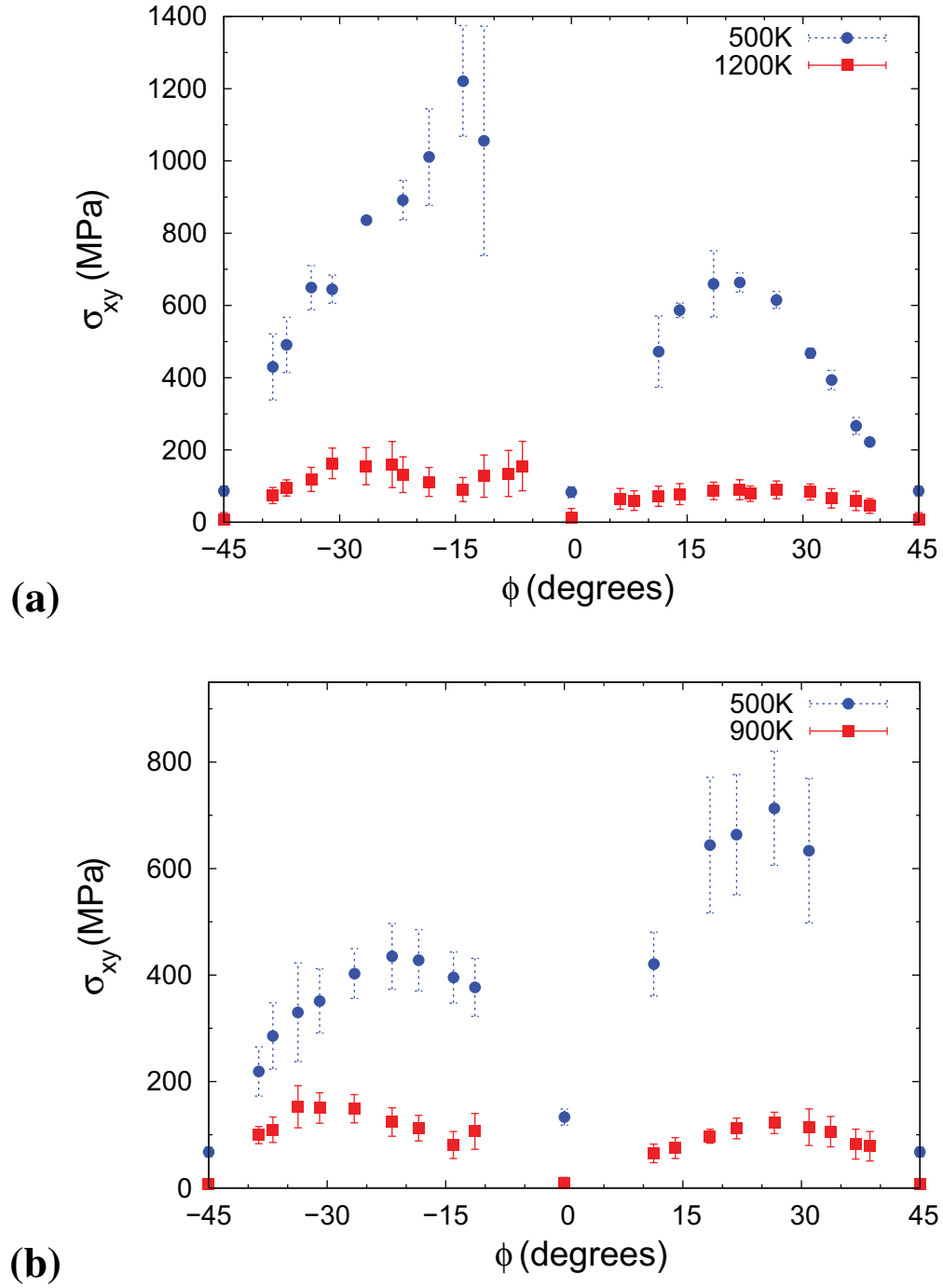


Figure 16: Steady-state shear stress as a function of inclination angle for GBs with the tilt angle $\theta = 16.26^\circ$. (a) Results for Cu. (b) Results for Al. The simulation temperatures are indicated in the legends.

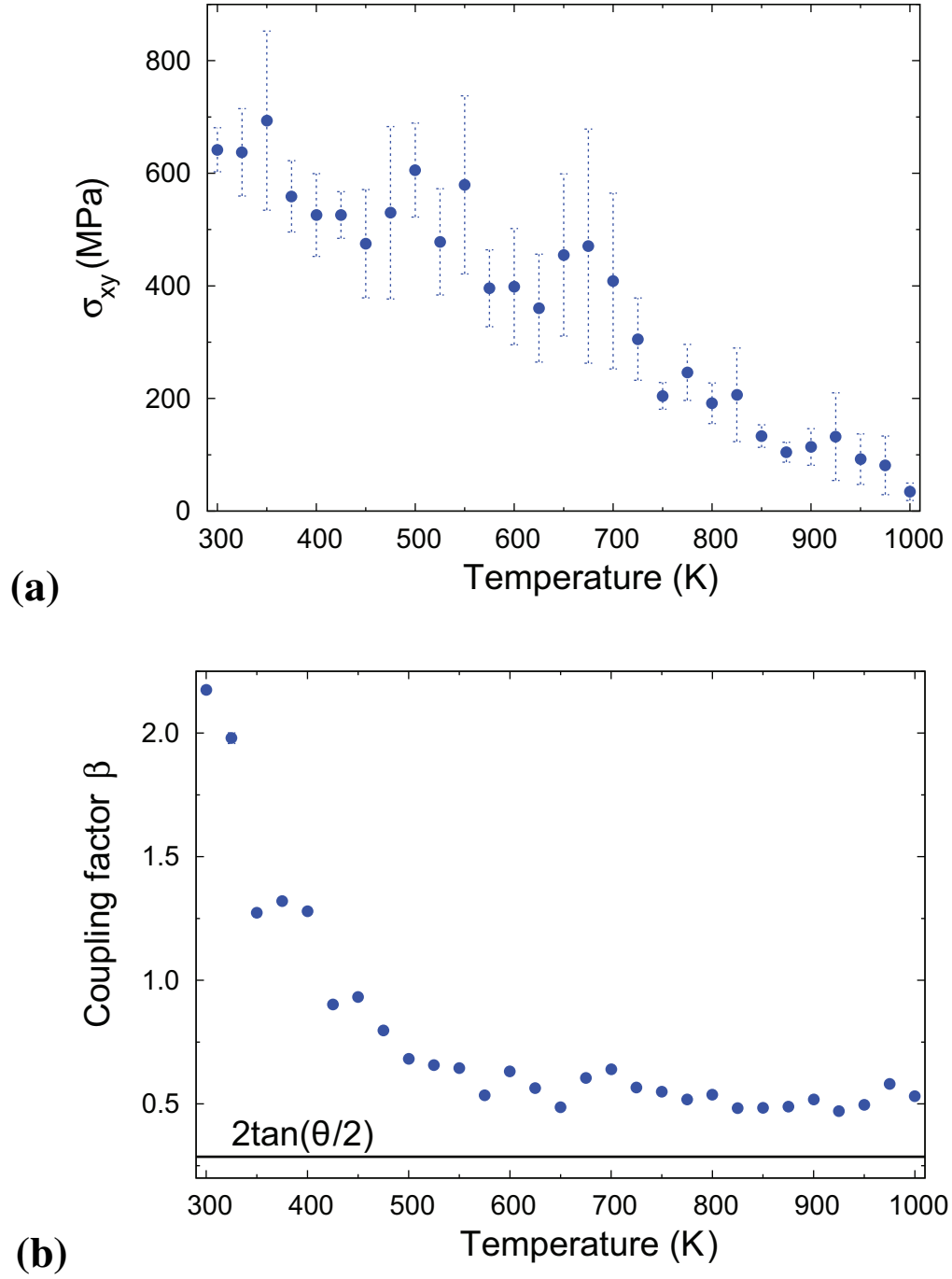


Figure 17: Shear stress (a) and coupling factor (b) as functions of temperature for an Al GB with $\theta = 16.26^\circ$ and $\phi = -18.44^\circ$. In (b), the horizontal line indicates the ideal coupling factor.

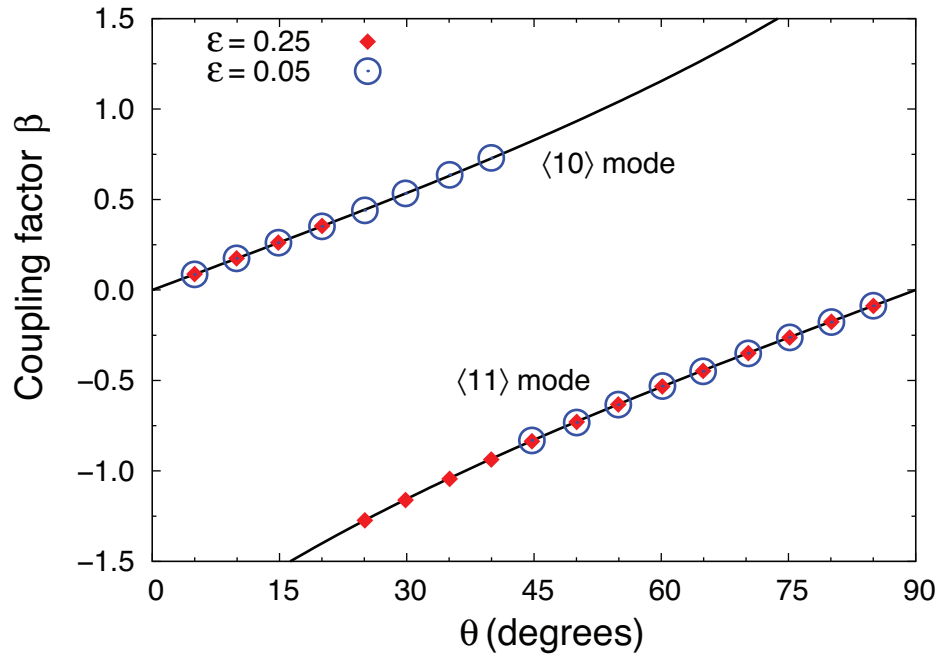


Figure 18: Coupling factor of symmetrical tilt GBs as a function of misorientation angle obtained by PFC simulations with $\epsilon = 0.25$ and $\epsilon = 0.05$. The lines indicate theoretical predictions [4] for two coupling modes.

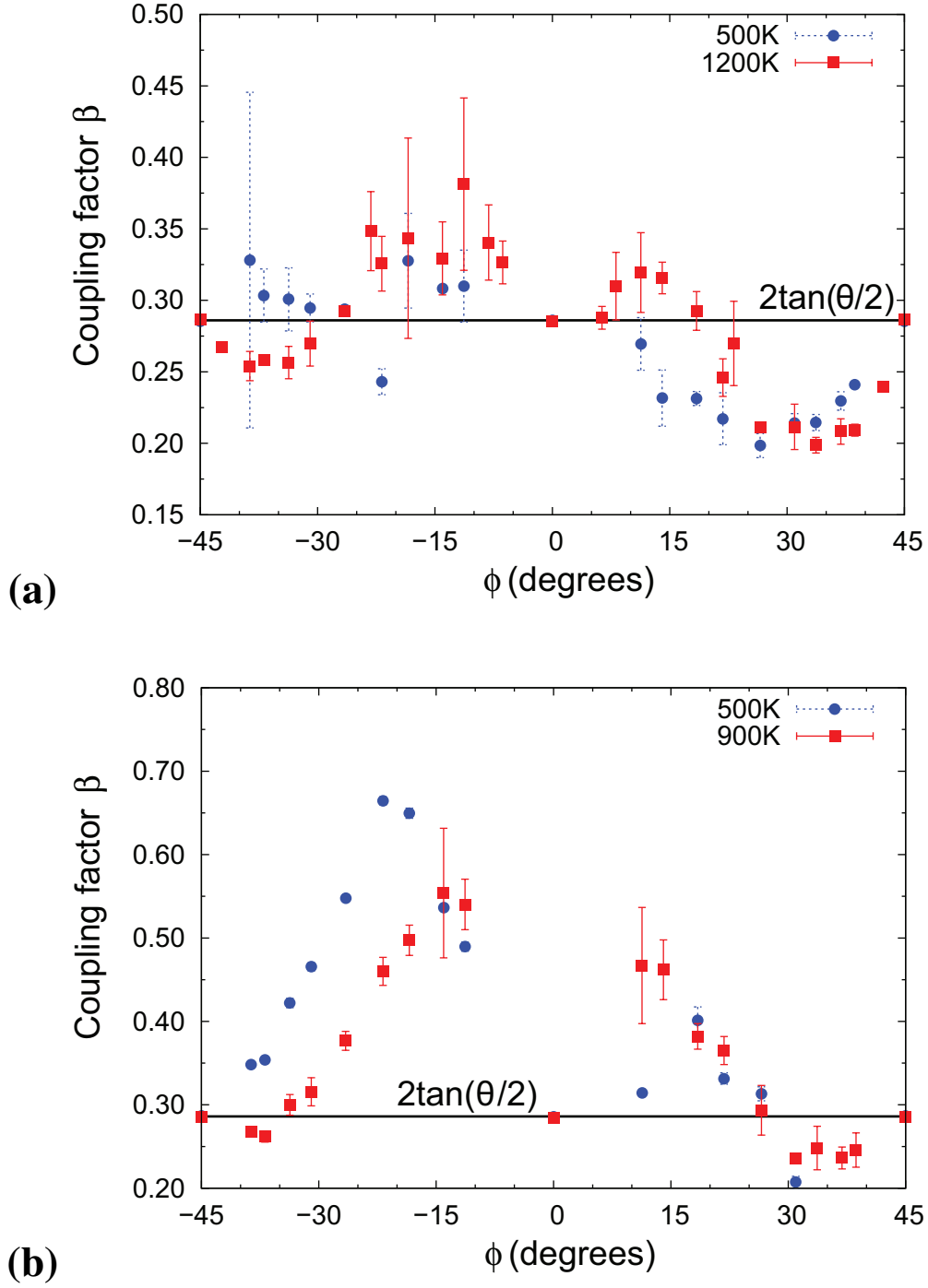


Figure 19: MD simulation results for the coupling factor of asymmetrical GBs in (a) Cu and (b) Al with $\theta = 16.26^\circ$ as a function of the inclination angle ϕ . The simulation temperatures are indicated in the legends. The horizontal line indicates the ideal coupling factor.

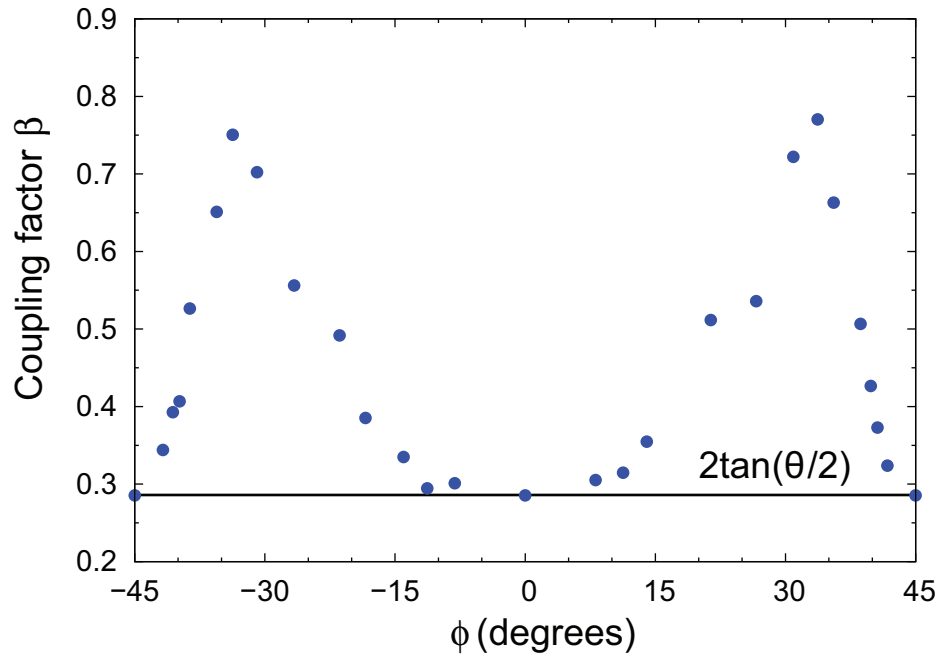


Figure 20: PFC results for the coupling factor of asymmetrical GBs with $\theta = 16.26^\circ$ as a function of the inclination angle ϕ . The horizontal line indicates the ideal coupling factor.

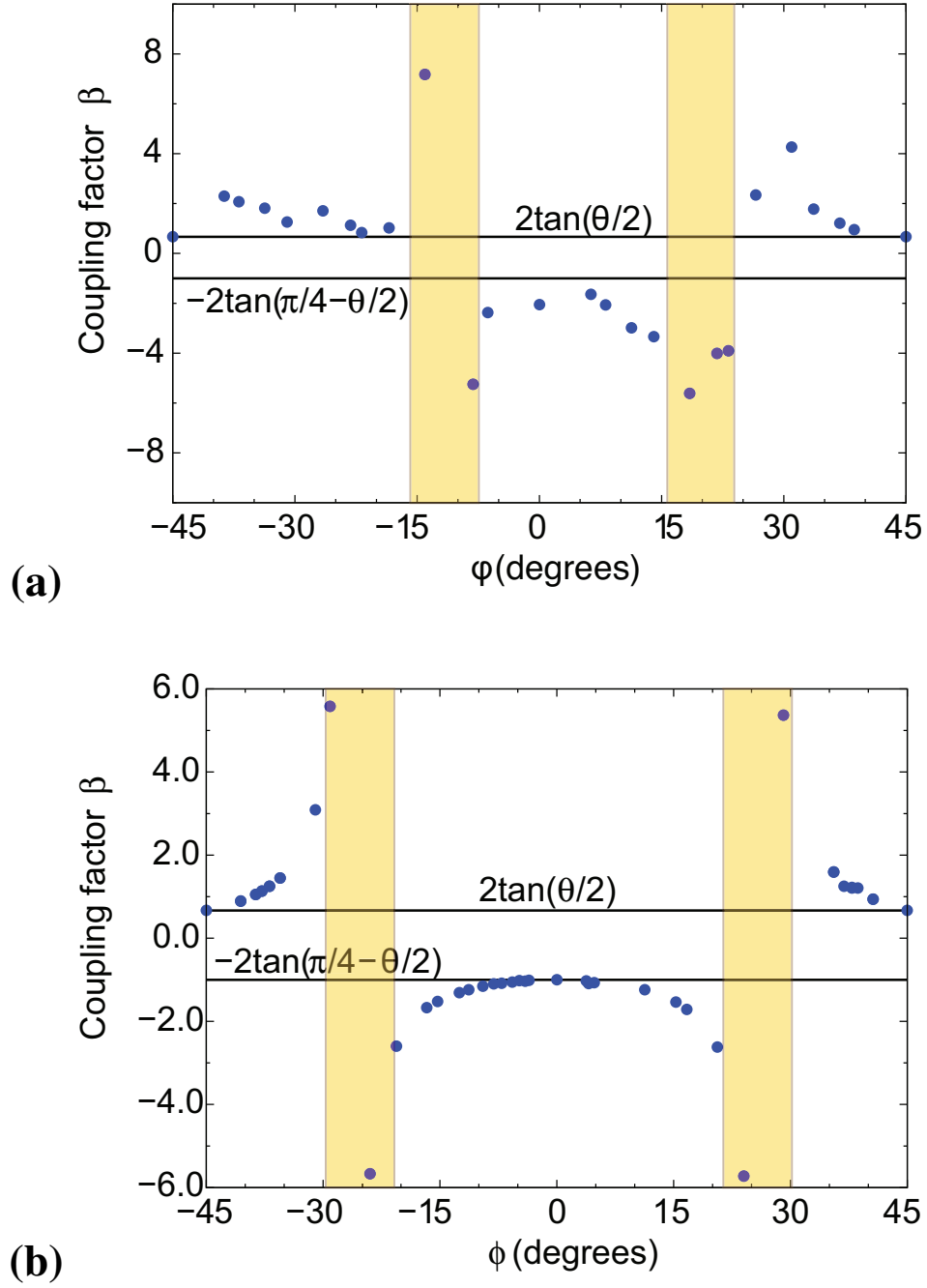


Figure 21: MD simulation results for Cu at 800 K (a) and PFC simulation results (b) for the coupling factor of asymmetrical GBs with $\theta = 36.87^\circ$ as a function of the inclination angle ϕ . The horizontal lines indicate the ideal coupling factors for two coupling modes. The shaded stripes indicate approximate regions in which the coupling factor switches between the modes.

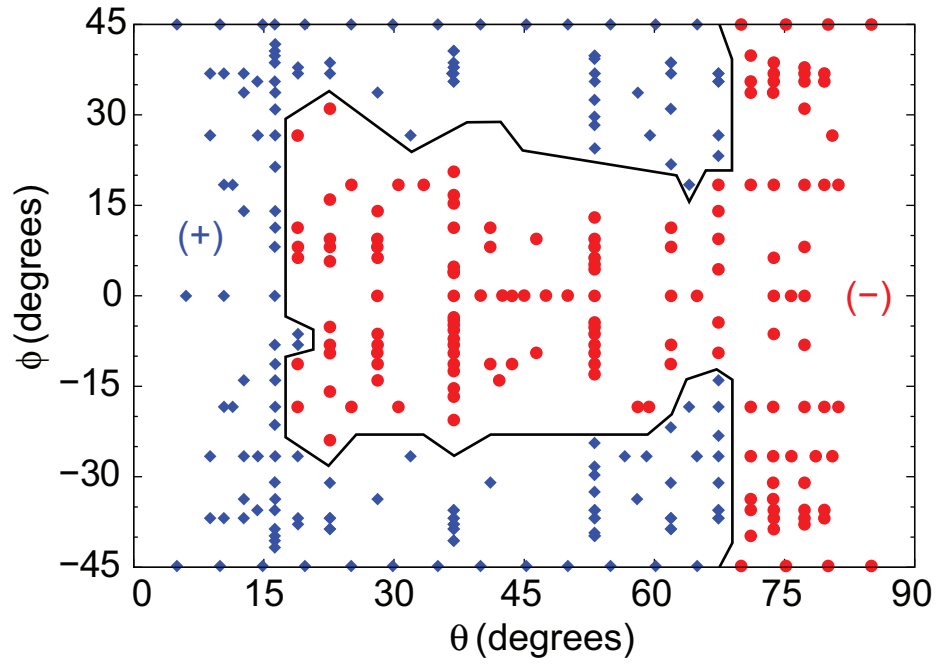


Figure 22: Summary of PFC calculations of the coupling factor for asymmetrical GBs. The diamond and circle symbols indicate positive and negative β , respectively. The line outlines the approximate boundary between the two coupling modes with different signs of β .